# A Two-Dimensional Diabatic Isopycnal Model—Simulating the Coastal Upwelling Front

E-CHIEN FOO[1]

*Meteorology Annex, Florida State University, Tallahassee 32306*

(Manuscript received 1 August 1980, in final form 3 February 1981)

ABSTRACT

A two-dimensional diabatic isopycnal model is designed to study coastal upwelling. The diabatic effect is represented by vertical mixing of the density field. Vertical eddy coefficients are determined by either a Richardson-number-dependent formula or a diagnostic second-order-moment closure turbulence model.

Some idealized coastal upwelling cases are studied. The results show that in a frontal zone, not only the density and velocity, but also the mixing intensity develop strong spatial variability. By using the turbulence model, sharp boundaries exist between the fully turbulent and quiescent regions. The thermal wind relation is greatly affected by turbulent mixing. Besides the effect of vertical diffusion of longshore momentum as suggested by one-dimensional models, vertical diffusion of density at a different rate horizontally has a strong effect on the thermal wind balance. Localized turbulent mixing will change the horizontal density gradient of its surrounding areas. As a result, strong upwelling develops in the region where turbulent intensity is maximum. During an upwelling event, turbulence first occurs at the inshore side of the surface front. Because of upwelling and downward diffusion of heat, the surface front is intensified at its offshore side. When the Richardson-number-dependent formula is used to calculate eddy coefficients, mixing occurs over a wider region; thus, no surface front develops.

## 1. Introduction

The combining detailed surface temperature and velocity information in an oceanic numerical model has been a difficult problem for modelers. The coarse resolution both in the vertical and horizontal directions prevents accurate estimation of surface properties. Vertical mixing near the surface, which is responsible for transporting the surface forcing and heating into the interior or back to the atmosphere, cannot be simulated adequately.

One-dimensional mixed layer models have been developed (Kraus and Turner, 1967; Pollard *et al.*, 1973; Niiler, 1975; Mellor and Durbin, 1975; Garwood, 1977) to improve vertical resolution near the surface. Certain success has been achieved in simulating temperature changes due to wind effects over time periods of a few days (Denman, 1973; Gargett *et al.*, 1979; Price *et al.*, 1978) or heating effects over annual cycles (Thompson, 1976). However, extending these models to several dimensions and combining them dynamically with circulation models is not straightforward. De Szoeke (1980) and Roisin (1980) both treated two-dimensional mixed layer problems over a stratified ocean but neglected the interior geostrophic current. Clancy and Martin (1979) designed a predictive model for surface temperature and salinity for the world ocean using a linear combination of geostrophic and Ekman currents. The processes of diabatic turbulence and geostrophic adjustment are treated independently and the interaction between them is excluded.

The surface structure of oceanic fronts has not been predicted to the same accuracy as its atmospheric counterpart. Although some of the deficiency is due to inadequate models and data, other reasons include the strong influence of the surface layer which responds to atmospheric forcing. In atmospheric fronts, the surface layer plays a more passive role.

Atmospheric studies show that frontogenesis usually takes place at the low pressure (warm) portion of an amplifying wave. Considering a zonally stable jet or portion of the wave where fronts develop, frontogenesis can be treated as a two-dimensional process influenced by a deformation field with a length scale much larger than the frontal scale. Hoskins and Bretherton (1972) used a barotropic convergent deformation field to induce frontogenesis. By using geostrophic coordinates, the governing equation becomes linear. Nonlinearity comes in only during coordinate transformation. Therefore, analytical solutions can be carried to the stage where surface temperature discontinuity takes

[1] Present affiliation: Exxon Production Research Company, Houston, TX 77001.

0022-3670/81/050604-23$09.75

place. For an Eady problem, the vertical shear of the mean jet is used as the deformation field to generate the front in the meridional direction. Orlanski and Ross (1977) applied a crossfront shear motion on an existing front. With the vertical shear in the direction opposite to the isotherms, secondary convergence develops near the surface which intensifies the front. Therefore, under a frontogenetically favorable field, nonlinearity works to speed up the process.

Pedlosky (1978) used a similar approach to that of Hoskins and Bretherton (1972) to study coastal upwelling. The upwelling current, which compensates the offshore Ekman transport, is used as the deformation field. A surface density front develops along the coast a few days after the onset of favorable winds.

Hoskins and Bretherton (1972) pointed out that the Richardson number at the frontal region must drop below its critical value before the discontinuity develops. Therefore, the effect of turbulence cannot be neglected during frontogenesis. Pedlosky (1978) further addresses the importance of surface boundary-layer dynamics in coastal frontogenesis. The vertical flux of fluid into the surface layer and the change of deformation field by including the surface Ekman transport might significantly alter the frontal structure.

This study focuses on oceanic frontogenesis. Therefore, an isopycnal coordinate model is implemented. The advantages of using isopycnal coordinates for frontal study has been addressed by Starr (1945) and Bleck and Boudra (1981). However, this coordinate system becomes cumbersome when it intersects boundaries which is usually the case with an oceanic front. Bleck and Boudra (1981) avoided intersection by using a generalized coordinate system. A minimum separation between vertical grid points is enforced by a mathematical formula. The coordinate surface changes gradually from isopycnal to Eulerian both in space and in time.

A different approach has been chosen in this study. The coordinate system is allowed to change suddenly from isopycnal coordinates to non-isopycnal coordinates along the physical boundary defined by the base of a well-mixed boundary layer.

The first situation considered in the model development deals with the evolution of a coastal upwelling front under wind forcing. The wind provides 1) the energy source for the system, 2) the deformation field through Ekman pumping and 3) turbulent mixing. The decision was made to first study coastal upwelling based on the following considerations: 1) it includes both mesoscale and frontal scale dynamics; 2) the front is trapped along the coast which allows it to be represented by a two-dimensional model; 3) simple lateral boundary conditions are chosen; and 4) the time for frontogenesis is short compared to open ocean frontogenesis even from an initial state of rest. These considerations allow a substantial decrease in the grid size and simulation time.

Pedlosky (1978) suggested that the formation of surface front during an upwelling event may be subject to strong influence of surface Ekman transport and turbulence. It seems to be the case in the field observation, as a surface front is not always observed during upwelling events. Those who favor the concept of double-cell circulation emphasize the existence of an upwelling front (Mooers *et al.*, 1976; Wroblewsky, 1977; Johnson, 1981) and strong mixing at the base of it (Wang and Mooers, 1977; Curtin, 1979; Johnson, 1981). Direct current measurement in Cyclesonde data (Johnson *et al.*, 1976; Johnson and Johnson, 1979) support these ideas. On the other hand, those who doubt double-cell phenomena argue that the surface front intensifies during relaxation stage instead of upwelling stage (Halpern, 1976). Fixed current-meter data suggest single-cell circulation (Hamilton *et al.*, 1977). Curtin (1979) shows that during the upwelling period, the surface front has moderate intensity with longshore uniformity, while in the relaxation stage, the front intensified and develops two-dimensional irregularity. Due to three-dimensional and transient processes over the upwelling region, the double cell circulation cannot be proved or disproved absolutely by direct observation. However, it suggests that frontal structure and turbulence distribution are critical to the overall circulation pattern.

Wroblewsky (1977) generated a double-cell circulation with a two-layer model (Thompson, 1974) by including interfacial friction. The same circulation was obtained by Endoh (1977) with a continuously stratified model containing a sharp pycnocline. Matsuno *et al.* (1978) started with a pycnocline at the surface. A double-cell circulation develops which intensifies the surface density gradient in certain areas within the initial surface front. These two continuously stratified models use weak density diffusion to prevent the front from spreading while momentum is allowed to diffuse. Hamilton and Rattray (1978) used Richardson number related vertical eddy coefficients which yield diffusion and viscosity coefficients of comparable magnitudes. Vertical mixing dominates near the surface; neither frontal structure nor organized interior circulation develops. The discrepancies between the Matsuno *et al.* (1978) and Hamilton and Rattray (1978) models cannot be explained easily because of different initial and boundary conditions involved. However, it suggests that density diffusion might erode a sharp front and prevent its related circulation pattern.

It is well known from one-dimensional models that sharp gradients of eddy coefficients may sometimes

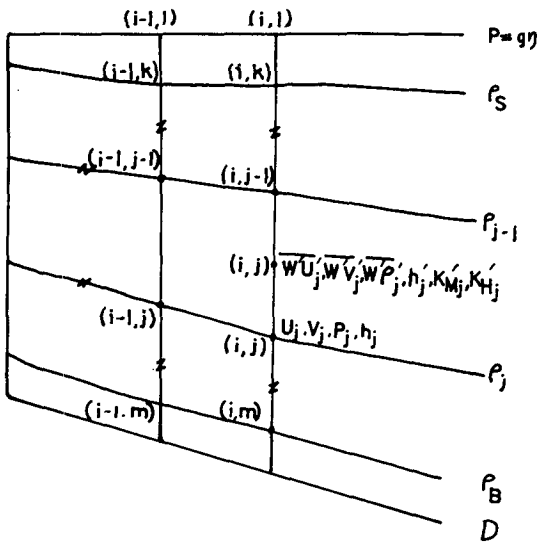


FIG. 1. The nonstaggered version of grid layout of the model. Only two interior grid levels and the surface and bottom boundary layers are shown. Indices in parentheses indicate the grid location. Parameters are defined at the location as indicated. For the staggered version, the horizontal velocity is defined one-half grid distance to the right.

intensify an existing pycnocline rather than diffuse it. In a frontal region, the turbulence shows spatial inhomogeneity (Curtin, 1979). Through the dynamical interaction between the turbulent mixing and the thermal wind balance, this inhomogeneity will have a profound effect in the frontal zone.

In order to generate a sharp boundary between the fully turbulent and quiescent regions, a sophisticated second-order moment closure turbulence model is used to estimate vertical eddy coefficients. This approach turns out to be relevant to frontal circulation. Turbulent regions become localized both vertically and horizontally. Divergence develops in the mixed layer over the column undergoing turbulent mixing. Strong upwelling develops which changes the overall upwelling pattern and induces closed circulation. The surface front is intensified by the mixing process.

Using Munk and Anderson's formula to estimate vertical eddy coefficients as suggested by Hamilton and Rattray (1978), the present model develops similar density structure without a surface front after simulation for several days. The frontal circulation is very diffuse.

## 2. Model

In this study isopycnal coordinates, which improve the vertical grid resolution in frontal regions in a natural manner, are used. In order to achieve the same vertical resolution in a frontal region with Cartesian coordinates, one needs a much smaller grid spacing over the whole model domain. Furthermore, the isopycnal surface is the surface of mixing for eddy scales larger than three-dimensional turbulence due to the existence of stratification. By using this coordinate system, false numerical horizontal diffusion of both heat and momentum across a frontal zone, typical of Cartesian coordinates, can be avoided.

Isopycnal coordinates are no longer material in a diabatic ocean. Although the velocity field in isopycnal coordinates becomes three dimensional in a diabatic region, the vertical movement is better resolved in these coordinates than in the Cartesian coordinates.

Two slablike boundary layers are used at the surface and bottom representing the well-mixed regions. For convenience of terminology, these homogeneous layers will be called mixed layers henceforth. However, it must be kept in mind that these layers are different from those ordinarily defined as mixed layers, which include the entrainment zone. In this model, the entrainment zone is part of the interior isopycnal coordinate domain.

### *a. Structure of the model*

Two interfaces between the mixed layers and the interior together with fixed density surfaces are used as grid levels. The density and velocity field are assumed to be constant in the mixed layers and vary linearly between adjacent vertical grid levels.

Fig. 1 shows the grid layout for the variables. The index $i = 1, \ldots, N$, indicates the horizontal grid location running from left to right. The index $j = 1, \ldots, M$, indicates the vertical grid running from top to bottom. The variables $u_j$, $v_j$, $h_j$, $\rho_j$ and $P_j$ are the horizontal cross-shelf velocity, longshore velocity, depth, density and pressure at level $j$. $\overline{w'u_j'}$, $\overline{w'v_j'}$, $\overline{w'\rho_j'}$, $K'_{Hj}$ and $K'_{Mj}$ are the vertical Reynolds fluxes and eddy coefficients at the midpoint of level $j$ and $j - 1$. The depth of that point is $h_j'$.

The arrangement of the vertical grid index needs further explanation. The subscript $k$ indicates the variables at the interface between the surface mixed layer and the interior. The subscript $m$ indicates the variables at the interface between the bottom mixed layer and the interior. Isopycnal grid levels go from $k + 1$ to $m - 1$. The value of $k$ and $m$ are determined by comparing the mixed-layer density with the density of each vertical grid levels. For instance, if $\rho_S$ is between $\rho_j$ and $\rho_{j-1}$, $k$ will be assigned a value $j - 1$. On the other hand, if $\rho_B$ is between $\rho_j$ and $\rho_{j-1}$, $m$ will be assigned a value $j$. The variables at $j = 2, \ldots, k - 1$, and $j = m + 1, \ldots, M$, are dummies.

In the mixed layer, the density changes with time by diabatic effects and horizontal advection. An interior grid point may disappear or reappear due to the change of mixed-layer density. For instance, if

the density of the surface mixed layer becomes larger than the density of the adjacent interior grid point $\rho_S > \rho_{k+1}$, this point is allowed to merge into the mixed layer and is excluded from the active prediction procedure. A new $k$ value equal to the previous $k + 1$ will be assigned as the mixed-layer index. On the other hand, with the decrease of the mixed-layer density $\rho_S < \rho_k$, a vertical grid point $k$ may reappear on an isopycnal grid level, the variables at that point will then be allowed to evolve independently. The variation of $m$ can be determined in the same way.

Due to the existence of the horizontal density gradient in the mixed layer, both $k$ and $m$ are functions of horizontal grid index $i$. The horizontal gradient evaluated at a grid point $(i, j)$ will be applied along a constant $j$ surface if $k(i) < j < m(i)$. If $j = k(i)$ or $j = m(i)$, the horizontal gradient will be applied along the interface of the surface or bottom mixed layer, respectively.

### b. Governing equations

Due to different assumptions made for the mixed layers and the interior domain, separate governing equations have to be derived for each.

#### INTERIOR

The following equations are derived from Bleck (1978) by including diabatic vertical mixing:

$$\frac{\partial u_j}{\partial t} + u_j \frac{\partial u_j}{\partial x} + \dot{\rho}_j \frac{\partial u_j}{\partial \rho} = A_M \frac{\partial^2 u_j}{\partial x^2} + \frac{\partial \rho}{\partial h} \frac{\partial}{\partial \rho}\left(K'_{Mj} \frac{\partial u_j}{\partial \rho}\right) - \frac{\partial M_j}{\partial x} + f v_j \quad (2.1)$$

$$\frac{\partial v_j}{\partial t} + u_j \frac{\partial v_j}{\partial x} + \dot{\rho}_j \frac{\partial v_j}{\partial \rho} = A_M \frac{\partial^2 v_j}{\partial x^2} + \frac{\partial \rho}{\partial h} \frac{\partial}{\partial \rho}\left(K'_{Mj} \frac{\partial v_j}{\partial \rho}\right) - \frac{\partial M_j}{\partial y} - f u_j \quad (2.2)$$

$$M_j = P_j \rho_j^{-1} + g h_j \quad (2.3)$$

$$\begin{pmatrix} K'_{Mj} \\ K'_{Hj} \end{pmatrix} = \begin{pmatrix} K_{Mj} \\ K_{Hj} \end{pmatrix} \frac{\partial \rho_j}{\partial h} \quad (2.4)$$

$$\dot{\rho}_j = \frac{d\rho}{dt} = \frac{\partial}{\partial h} K_{Hj} \frac{\partial \rho}{\partial h} = \frac{\partial \rho}{\partial h} \frac{\partial}{\partial \rho} K'_{Hj} \quad (2.5)$$

$$\frac{\partial P_j}{\partial t} = \sum_{i=2}^{j} \frac{\partial}{\partial x} (P_i - P_{i-1})(u_i + u_{i-1})/2 + \dot{\rho}_j \frac{\partial P_j}{\partial \rho} + A_H \frac{\partial^2 P_j}{\partial x^2} . \quad (2.6)$$

Where $h$ is the depth, $A_M$ and $A_H$ are the horizontal eddy coefficients, $K_{Mj}$ and $K_{Hj}$ are the vertical eddy coefficients (in cm$^2$ s$^{-1}$), $K'_{Mj}$ and $K'_{Hj}$ are derived from $K_{Mj}$ and $K_{Hj}$ by Eq. (2.4) to fit the new coordinates.

Eqs. (2.1) and (2.2) are momentum equations, $M$ is the Montgomery potential and is defined by (2.3). Eq. (2.5) is the thermodynamic equation. The diabatic effect is generated by vertical mixing of the density field. This mixing process induces a vertical velocity in this coordinate system representing a mass flux across the density surfaces. It also appears in the advection term of the momentum equation. Eq. (2.6) is the vertically integrated continuity equation above level $j$. The first term on the right-hand side represents the integrated horizontal divergence. The second term represents the vertical transport across the level $j$. The last term is the horizontal thickness diffusion. Some modifications on the equations are needed for the boundary layers (see Appendix A).

### c. Eddy coefficients

One major concern of this study is to understand the effect of turbulence on frontal dynamics. The horizontal eddy coefficients, $A_M$ and $A_H$, are assumed constant. The vertical eddy coefficients are assumed to be related to the mean velocity and density field in order to give a better estimation of turbulence intensity. A simplified diagnostic second order moment closure turbulent energy model derived from Worthem and Mellor's (1980) original model is used. In addition, a Richardson-number-dependent formula derived by Munk and Anderson (1948) is used for comparison purposes.

#### 1) RICHARDSON-NUMBER-DEPENDENT FORMULA

Munk and Anderson (1948) used experimental data to derive the following empirical eddy coefficient formulas.

$$K_M = 5 + 50(1 + 10\ \mathrm{Ri})^{-1/2}, \quad (2.7)$$

$$K_H = 50(1 + 3.3\ \mathrm{Ri})^{-2/3}, \quad (2.8)$$

where Ri is the Richardson number. The coefficients are adopted from Hamilton and Rattray (1978). In a stable region where Ri is large, a background momentum diffusion coefficient of 5 cm$^2$ s$^{-1}$ is assumed without its density diffusion counterpart. In a fully turbulent region, Ri drops and the eddy coefficients approach the maximum value of 55 and 50 cm$^2$ s$^{-1}$, respectively.

#### 2) SECOND-ORDER MOMENT CLOSURE SCHEME

Worthem and Mellor (1980) used a prediction equation to determine the turbulent kinetic energy and turbulence length scale. In this model, a simplified diagnostic approach is used to estimate the eddy coefficients. Turbulence diffusion and dissipation are assumed to be balanced by production, i.e.,

$$\frac{\partial}{\partial h}\left(K_M \frac{\partial q^2}{\partial h}\right) = -K_M\left(\frac{\partial u}{\partial h}\right)^2 - K_M\left(\frac{\partial v}{\partial h}\right)^2 - K_H g\rho^{-1}\frac{\partial \rho}{\partial h} + \frac{2q^3}{B_1 l}, \quad (2.9)$$

where $q^2$ is the turbulent kinetic energy, $B_1$ is an empirical constant, and $l$ is the mixing-length scale which has to be determined by an empirical equation. No time derivative term is involved. The eddy coefficients are determined by turbulent energy, mean field gradient and turbulent length scale:

$$K_M = lqS_M, \quad (2.10)$$

$$K_H = lqS_H, \quad (2.11)$$

$$S_M = f\left(l, q, \frac{\partial \rho}{\partial h}, \frac{\partial u}{\partial h}, \frac{\partial v}{\partial h}\right), \quad (2.12)$$

$$S_H = g\left(l, q, \frac{\partial \rho}{\partial h}, \frac{\partial u}{\partial h}, \frac{\partial v}{\partial h}\right), \quad (2.13)$$

where the function $f$ and $g$ are given in Worthem and Mellor (1980). The formulation of the turbulence length scale $l$ is given in Appendix B.

### d. Longshore pressure gradient

In an $f$-plane system without any longshore gradient, the horizontal transport outside the upwelling zone and under uniform wind stress is

$$V = \left(\frac{\tau_y}{C_d}\right)^{1/2}, \quad (2.14)$$

where $\tau_y$ is the longshore wind stress and $C_d$ the bottom drag coefficient. The outflow in the surface Ekman layer is entirely balanced by an inflow at the bottom boundary. In the open ocean, the geostrophically balanced velocity field is basically a Sverdrup transport, which is much weaker than the velocity in (2.35) and cannot induce any effective bottom boundary current. Thus, the surface Ekman transport should be balanced by an interior counterflow. Solving the upwelling problem on an $f$-plane without any longshore pressure gradient to counteract the open-ocean wind stress may thus turn out to be unrealistic. In the absence of the strong bottom boundary-layer inflow, this longshore pressure gradient also serves the purpose of balancing the surface outflow by an inflow from the whole water column. Hurlburt and Thompson (1973) and Garvine (1974) connected the large-scale interior solution to the coastal region with a $\beta$-plane adjustment. The existence of a finite $\beta$ allows a Sverdrup region to exist, i.e.,

$$\int v dh = \beta^{-1}\nabla \times \boldsymbol{\tau} = \beta^{-1}\frac{\partial \tau_y}{\partial x}. \quad (2.15)$$

By assuming that (Garvine, 1974) 1) the bottom boundary-layer transport can be neglected, 2) a mass balance exists in the $x$-$z$ plane and 3) the ocean interior is in geostrophic balance, the longshore pressure gradient can be determined by integrating the vorticity equation across the ocean to the open boundary $x_0$,

$$\left.\frac{\partial P}{\partial y}\right|_{x_0} = f^{-1}\int_0^{x_0} \beta v dx = \frac{\tau_y|_{x_0}}{D_0}, \quad (2.16)$$

where $D_0$ is the water depth. The pressure force is exactly balanced by the wind stress at $x_0$.

The longshore pressure gradient over the model domain is determined as

$$\frac{\partial P}{\partial y} = \left.\frac{\partial P}{\partial y}\right|_{x_0} + f^{-1}\int_{x_0}^{x} \beta v' dx, \quad (2.17)$$

where $v'$ is the surface longshore geostrophic velocity,

$$v' = V + \frac{\beta}{f}\left(\int \frac{\partial M}{\partial x} dh\right)D^{-1}, \quad (2.18)$$

which includes the barotropic velocity $V$ and the geostrophic baroclinic velocity. Garvine (1974) pointed out that the change of $\partial P/\partial y$ across the upwelling zone was ~5% based on observational data.

### e. Numerical implementation

#### 1) Integration scheme

An explicit leapfrog scheme is used for time integration. The vertical diffusion term is calculated with the Crank-Nicolson scheme. The vertical advection term and the horizontal advection of density in the mixed layer are calculated with an upstream spline interpolation technique (Mahrer and Pielke, 1978).

In order to resolve the fast response of a sudden wind change, a free surface is used to include the fast barotropic gravity wave mode. The horizontal velocity is divided into a barotropic part and a baroclinic part and updated with two different time scales. A short time step is used to calculate the barotropic mode which includes surface gravity waves, a longer time step is used to calculate the baroclinic mode. After each long time step, the baroclinic velocity is averaged vertically and its mean value is subtracted from the baroclinic and added to the barotropic component. See details in Appendix C.

#### 2) Boundary conditions

A free surface is assumed with the atmospheric pressure set to zero. At the rigid sidewall and bottom, the normal velocity is assumed to vanish. Free-slip and no-slip boundary conditions are used separately at the vertical wall. For the open ocean boundary ($i = N$), the surface height is defined as $\eta_N$

$= U_N(D/g)^{1/2}$ to give a transparent boundary for long gravity waves, suggested by Hamilton and Rattray (1978). The horizontal derivatives of all the variables are assumed to vanish at the open boundary. A sponge layer is assumed at the three horizontal grid points nearest the open boundary with increasing diffusion, i.e.,

$$\left.\begin{aligned} A_M(n) = A_H(N) &= 100A_M \\ A_M(N-1) = A_H(N-1) &= 20A_M \\ A_M(N-2) = A_H(N-2) &= 5A_M \end{aligned}\right\},$$

to suppress reflection from this boundary, $N$ is the grid number of the open boundary. The tendency term is not suppressed because wind forcing does not fall off near the boundary. Suppressing the tendency term would generate a convergence in the Ekman layer.

### *f. Diabatic effects*

The mean field has a much smaller vertical than horizontal scale. Turbulence events are determined mainly by the vertical variation of velocity and density. Therefore, it is reasonable to combine a one-dimensional turbulence kinetic energy model with a two or three-dimensional mean field model.

#### 1) CONNECTING THE TURBULENCE MODEL WITH THE ISOPYCNAL MODEL

The empirical constants involved in the turbulence model are determined from experimental data. It is impossible to convert this model in a straight-forward fashion from Cartesian coordinates into isopycnal coordinates. Hence, when the eddy coefficients are to be updated, the mean field profile is interpolated to Cartesian coordinates. Thereafter, the diagnostic turbulence model is applied. The resulting eddy coefficients are subsequently converted back to isopycnal coordinates.

The density and velocity field in the mixed layer is too coarsely defined with our computational grid to give any realistic turbulence estimation. Therefore, the turbulence model is applied only from the bottom of the mixed layer downward for a finite distance (50 m) to include the entrainment zone. A simplifying assumption will be made in the well-mixed layer to provide the upper boundary conditions for the turbulent model. The boundary values at the base of the mixed layer are defined as follows:

(i) Turbulent kinetic energy $q^2$ is assumed constant in the well-mixed constant stress layer; thus, the surface value (Worthem and Mellor, 1980) is used as the boundary condition $q^2 = \tau_y B_1^{2/3} \rho^{-1}$. This assumption sometimes underestimates the intensity of turbulence because upward diffusion and local shear production are excluded.

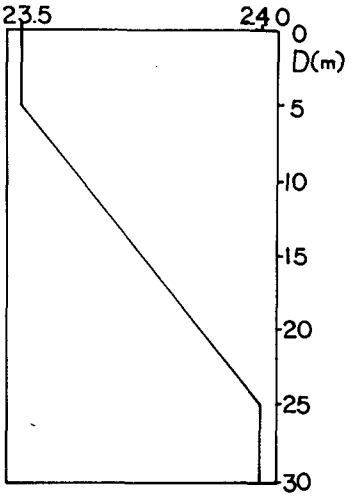


FIG. 2. The initial density structure of the water column for the one-dimensional wind mixing experiment.

(ii) The mixing length $l$ is assumed to be equal to $\kappa h_k$. The turbulent kinetic energy and mixing length will be defined differently during detrainment. They will be assigned background values.

With boundary values determined, the eddy coefficients can be evaluated and converted back to isopycnal coordinates.

#### 2) ONE-DIMENSIONAL MODEL SIMULATION AND ITS COMPARISON WITH MELLOR'S MODEL

A comparison test has been carried out on a one-dimensional version of the isopycnal model and Mellor's model to support the performance of this hybrid method. A constant wind stress of 1 dyn $cm^{-2}$ is applied over a non-rotational water column of 30 m depth with the initial density structure shown in Fig. 2. A uniform velocity of 10 cm $s^{-1}$ is assumed initially.

In order to simulate velocity shear in the mixed layer, an additional grid is added at the surface. Mixing is parameterized between the top and bottom of the mixed layer to give the appropriate shear as shown in Fig. 3. However, in the two-dimensional case, one cannot discriminate between the shear generated by surface stress or horizontal density gradient, applying this mixing parameter is not straightforward.

Figs. 3 and 4 give the progressive profiles of the velocity and density structure. They show very similar profiles and deepening rates. During the initial stage, Mellor's model takes longer for the turbulence to develop in the homogeneous layer. The velocity gradient is still concentrated near the surface after 4 h.

Due to the numerical method and vertical coordinates chosen for this model, momentum and mass are not automatically conserved. Therefore, it is

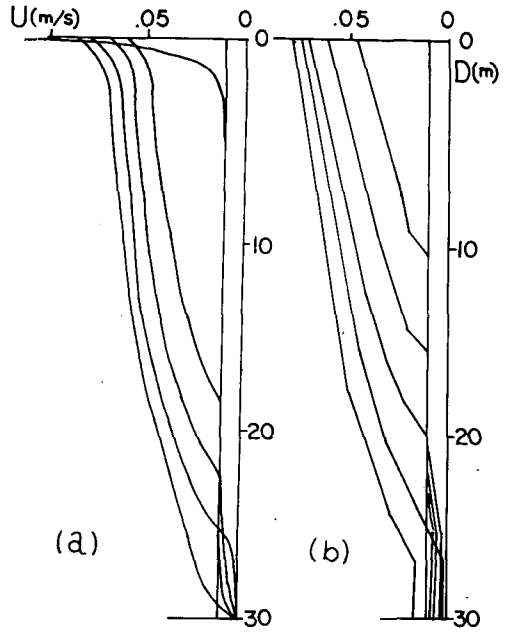


FIG. 3. The consecutive velocity profiles during mixing under constant wind stress for (a) Mellor's and (b) the hybrid model simulation. Each profile is separated by roughly 24 000 s.

necessary to check the conservation ability of this model through performance. Table 1 compares the conservation properties of these two models. The variable $R$ is defined as the difference between the mass of the water column and the mass of the same water column if filled with water of initial surface density,

$$R = \int \rho dh - \rho_{si} D,$$

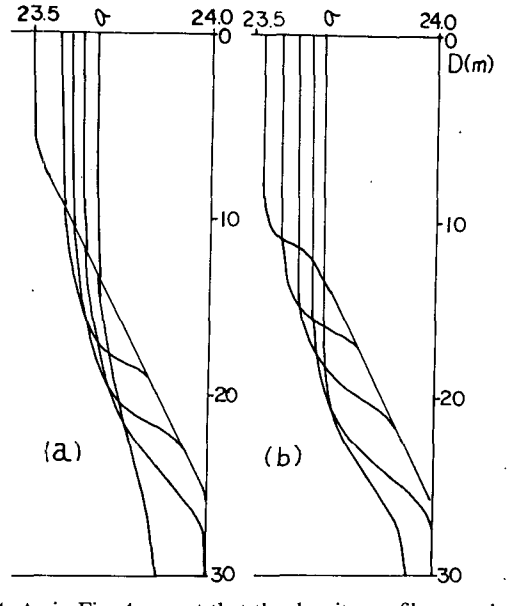


FIG. 4. As in Fig. 4 except that the density profiles are shown.

TABLE 1. The comparison between the hybrid model and Mellor's model for the conservation of momentum and heat.

| Mellor's model | | | | |
|---|---|---|---|---|
| Time (s) | $M1$ ($m^2\ s^{-1}$) | $M2$ ($m^2\ s^{-1}$) | $R_I$ ($g\ cm^{-2}$) | $R$ ($g\ cm^{-2}$) |
| 0 | 3.00 | 3.00 | 7.00 | 7.00 |
| 23 420 | 5.26 | 4.53 | 7.00 | 7.05 |
| 49 920 | 7.78 | 8.00 | 7.00 | 6.98 |
| 75 520 | 10.31 | 10.05 | 7.00 | 7.00 |
| 101 120 | 12.86 | 12.54 | 7.00 | 6.97 |
| 165 120 | | | 7.00 | 6.83 |
| **One-dimensional hybrid model** | | | | |
| Time (s) | $M1$ ($m^2\ s^{-1}$) | $M2$ ($m^2\ s^{-1}$) | $R_I$ ($g\ cm^{-2}$) | $R$ ($g\ cm^{-2}$) |
| 0 | 3.00 | 3.00 | 7.50 | 7.50 |
| 24 260 | 5.24 | 5.27 | 7.50 | 7.49 |
| 50 220 | 7.70 | 7.94 | 7.50 | 7.54 |
| 75 820 | 10.26 | 10.47 | 7.50 | 7.57 |
| 101 420 | 12.76 | 13.25 | 7.50 | 7.60 |
| 140 000 | | | 7.50 | 7.68 |

where subscript $si$ represents initial surface value and $D$ is the water depth. Our model shows a slight increase of $R$ as the mixed-layer deepens. After the whole water column becomes uniformly mixed, the final $R$ increases by 1.5%. Mellor's model shows a slight decrease of $R$ and a 2.5% change is obtained at the final stage.

The conservation of momentum can be determined by comparing the integrated boundary forcing with the actual momentum change. The boundary forcing includes the wind stress and the bottom friction. In the hybrid model, we use integration

$$M_1 = M_{in} + \int (\tau_S/\rho - C_d(U + u_m)^2)dt,$$

where $C_d$ is the drag coefficient and $(U + u_m)$ is the bottom velocity. $M_{in}$ is the initial integrated momentum. In Mellor's model, the bottom dissipation is estimated by

$$\tau_B = \frac{q_B^2}{q_S^2}\tau_S$$

and the integration of boundary forcing is

$$M_1 = M_{in} + \int (\tau_S - \tau_B)dt\rho^{-1}.$$

The variable $M_2$ is the actual integrated momentum of the water column, i.e.,

$$M_2 = \int udh$$

Table 1 gives both $M_1$ and $M_2$. The hybrid model shows 4% extra momentum in the system after 28.2 h, and Mellor's model shows 2% deficiency.

The turbulent kinetic energy and eddy coefficients in the entrainment zone have comparable magnitudes in both models. Fig. 5 gives the vertical profiles of $q^2$ and $K_M$, showing maximum values $\sim 1. \times 10^{-3}$ m$^2$ s$^{-2}$ and $2 \times 10^{-3}$ m$^2$ s$^{-1}$, respectively.

Judging from this test, the one-dimensional isopycnal model gives a reasonable estimation of the turbulence and deepening rate. Therefore, this hybrid method of calculating turbulence and mean field effects in different coordinates will be used in the two-dimensional model.

## 3. Results

A series of cases simulating coastal upwelling events have been studied. Certain conditions remain unchanged throughout the experiments. These conditions are as follows:

1) The model domain extends 40 km offshore and is bounded by a vertical sidewall, an open-ocean boundary, a free surface and a rigid bottom.

2) The initial stage is one of rest with horizontal density surfaces. No background geostrophic velocity is assumed.

3) The initial vertical density distribution can be inferred from Fig. 6 with an internal pycnocline centered $\sim 52$ m.

4) Two homogeneous boundary layers of 10 m vertical thickness are assumed to exist initially at the surface and bottom.

5) The wind stress longshore is assumed to be spatially uniform and to increase from zero to 1 dyn cm$^{-2}$ within 34 h; thereafter, it is kept constant.

Several experiments have been carried out to identify the effect of large-scale adjustment, topography, sidewall friction and vertical diffusion. Table 2 lists the different assumptions made in each separate case. Cases I–III are run for the purpose of identifying the effects of $\beta$-plane adjustment and sidewall friction. Case IV and following cases are run with a sloping bottom and a $\beta$ plane. Case VII deals particularly with the effect of Munk and Anderson's (1948) eddy coefficient formulation.

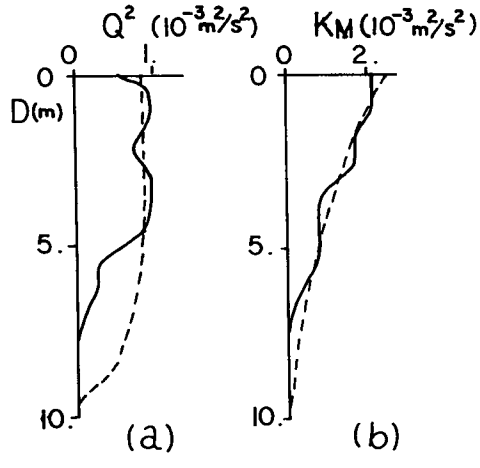


FIG. 5. The profiles of (a) turbulence kinetic energy and (b) eddy coefficient from the base of the well-mixed layer at 20.8 h. The origin represents the base of the mixed layer which has a depth of 13.6 m.

TABLE 2. List of conditions in case study.

| Case | Rotation | Sidewall | Bottom | Grid | Eddy coefficient |
|---|---|---|---|---|---|
| I | $\beta$ | non-slip | flat | staggered | turbulence* |
| II | $f$ | non-slip | flat | staggered | turbulence |
| III | $f$ | free-slip | flat | staggered | turbulence |
| IV | $\beta$ | non-slip | slope | non-staggered | turbulence |
| V | $\beta$ | non-slip | slope | non-staggered | Munk** |

* Eddy coefficients determined by turbulence model.
** Eddy coefficients determined by Munk and Anderson's formula.

A strong pycnocline is used to give some spatial inhomogeneity for the initiation of frontogenesis. Each case is run for about 150–200 h in real time. This is the time needed for the coastal jet to intensify and become turbulent and for the interior stable layer to surface. The frontal-scale circulation reaches its full strength at $\sim 150$ h. It should be pointed out that a finite domain model like the present one cannot be integrated for too long a time. The solution sooner or later is contaminated by boundary effects from the open ocean boundary. In addition, the model does not include adequate dynamic and thermodynamic processes to restore the system to its initial state.

### *a. Case I: β plane and flat bottom*

This case study is carried out on a $\beta$ plane with flat bottom and no-slip sidewall. The effect of $\beta$ plane adjustment is generated by including a longshore pressure gradient to balance the wind stress. This run is integrated for 170 h real time. A series of plots, Fig. 6–8 show the evolution of an upwelling event at different stages. Two plots are shown in each figure. The dashed lines are density surfaces with $0.1\sigma_t$ interval; every other line is a grid level. Plot (A) shows the longshore velocity; the solid lines indicate current flow into the plan of drawing and contour intervals are 10 cm s$^{-1}$. Plot (B) shows the crossfront streamfunction with contour interval of 0.1 m$^2$ s$^{-1}$; the solid lines indicate clockwise circulation. Fig. 6 shows the early stage of upwelling at 34.2 h at which time a clockwise circulation develops over most of the model domain. The upwelling region, which is defined as the area where the interior water rises into the surface layer, is concentrated in a narrow area. A weak counterclockwise circulation indicated by the negative streamfunction is formed near the coast. The crossfront circulation pattern basically resembles the linear analytical solution.

Fig. 7 shows the flow pattern at 102.6 h. The long-

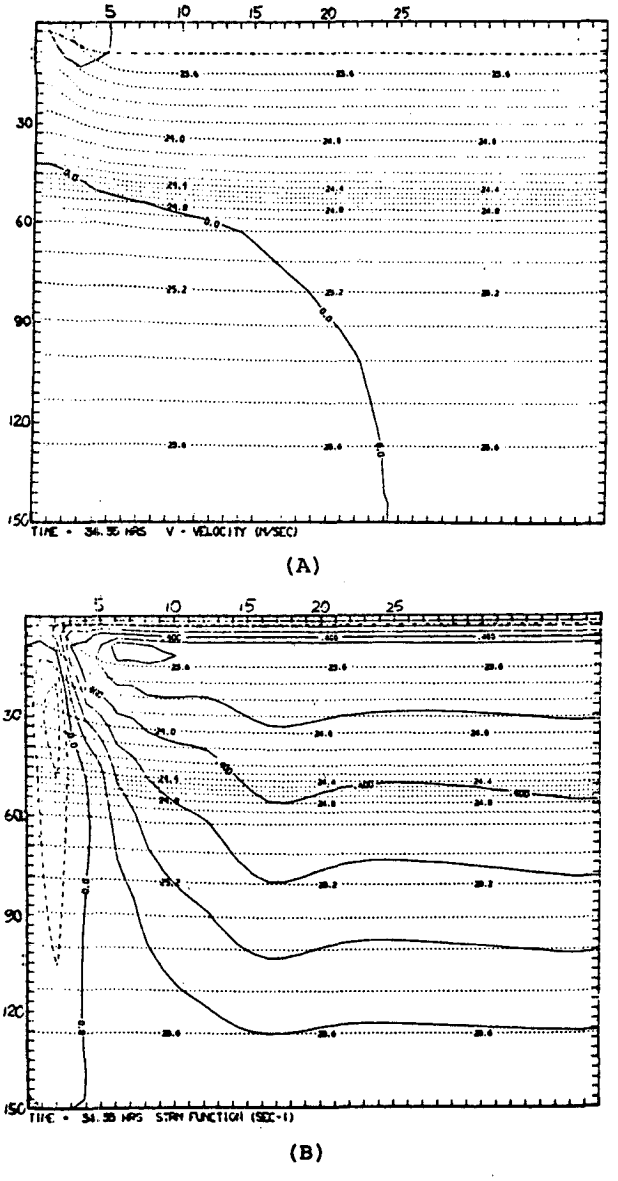


FIG. 6. The flow pattern for case I at 34.3 h; (a) the longshore velocity and (b) the crossfront streamfunction. The tick marks represent 1 km in the horizontal and 3 m in the vertical. The dashed curves at the left edge of plot (b) indicate counterclockwise circulation.

shore velocity already has developed to full strength. The pycnocline just reaches the mixed layer at the coast. The core of the current has accelerated to 42 cm $s^{-1}$ but stays near the coast; the countercurrent in the lower layers increases to over 10 cm $s^{-1}$.

Due to the intensification of the coastal jet and the mixed-layer density gradient, nonlinear advection of the momentum and density in the mixed layer can no longer be neglected. Additional crossfront transport develops in the mixed layer. A streamfunction maximum exists at 30 m depth and 12 km off the coast at the offshore side of the jet. The streamline pattern indicates that the upwelling region extends from this point to the coast while weak downwelling exists further offshore. This may be related to the pivot point found by Curtin (1979).

In the upwelling zone, the mixed-layer depth changes from its initial value. With the offshore advection of dense water, the mixed-layer thickens shoreward due to convective mixing. However, it thins sharply further inshore where strong upwelling takes over. Therefore, the mixed-layer depth shows a maximum 8 km off the coast.

At 170.9 h, the pycnocline surfaces and forms a surface front (see Fig. 8). The core of the coastal jet advects offshore with this front. Strong turbulent

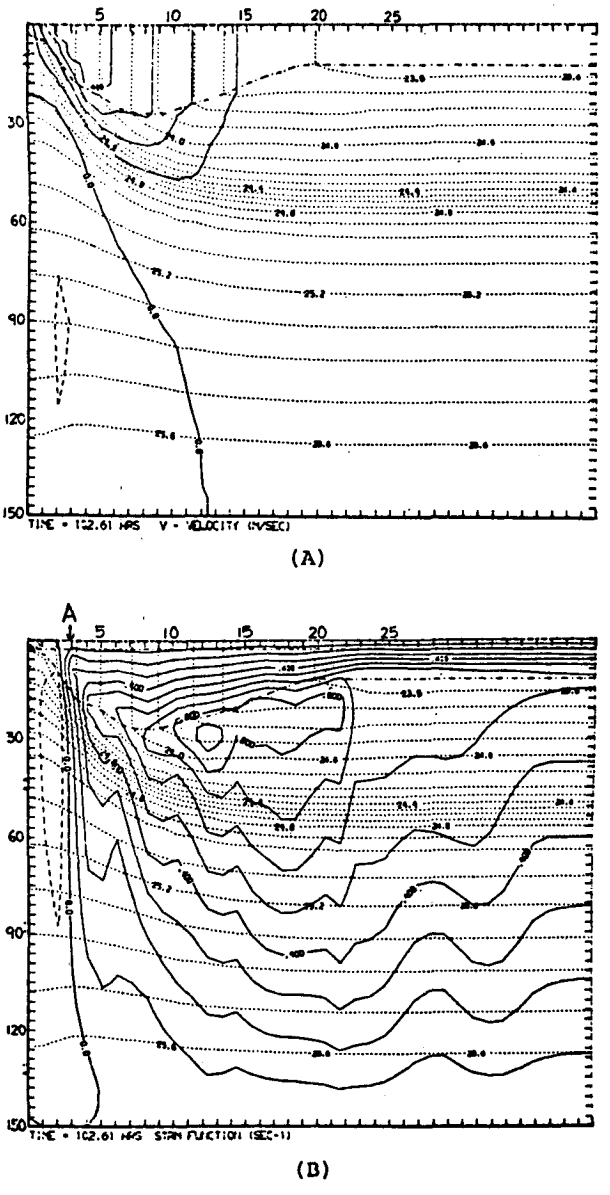


FIG. 7. The flow pattern for case I at 102.6 h. The dashed curve at the left edge of plot (a) indicates the undercurrent.

mixing is located at the inshore side of the jet and it develops certain localized phenomena around column B: 1) the mixed-layer density increases so quickly that the horizontal density gradient increases at the offshore side and decreases at the inshore side, thus intensifying the surface front; 2) the mixed-layer deepens and the interior density surfaces dip locally; 3) strong upwelling develops; 4) the velocity shear drops considerably in this column which causes the coastal jet to split into two; one along the coast and the other along the surface front; and 5) a clockwise circulation spins up at column C.

Two additional upwelling currents exist at columns A and D, and another clockwise circulation is located around column E.

### b. *Case II: F-plane and no-slip sidewall*

This case is compared with case I to demonstrate the effect of large-scale divergence adjustment. Fig. 9 gives the flow pattern at 102 h. Compared with Fig. 7, the longshore jet has a similar structure as in case I except that a barotropic velocity component is added. Without the pressure gradient to balance the wind stress, the barotropic velocity component accelerates with time. For a wind stress of 1 dyn $cm^{-2}$ and bottom drag coefficient of $1.5 \times 10^{-3}$, the steady-state longshore velocity outside the upwelling zone should be $V = (\tau_y/C_d)^{1/2} = 25.3$ cm $s^{-1}$. At 170 h, the $V$ velocity at the open boundary is 24 cm $s^{-1}$. The bottom boundary inflow almost balances the surface Ekman outflow at this time.

The cross-front circulation deviates from Case I as the inflow becomes more confined to the bottom boundary layer. At 102 h (see Fig. 9), a major part of the onshore transport is concentrated in the bottom boundary layer and then turns upward under the surface jet. This flow pattern induces a much larger upwelling velocity in the deep region along the coast than does the $\beta$-plane case. In 102 h the water is lifted an extra 8 m at 130 m depth. However, the difference decreases upward. In the upper region of the frontal zone, the circulation pattern looks similar to the $\beta$-plane case.

### c. *Case III: F-plane and free-slip sidewall*

Both free-slip and no-slip sidewall boundary conditions have been used in past numerical and theoretical models. It is interesting to compare the differences generated by these two conditions in the present model. Fig. 10 gives the free-slip flow pattern at 102 h. Comparing Figs. 7, 9 and 10, the difference of cross-front circulation between Fig. 7 and 9 is found primarily outside the hydrostatic boundary layer, while the difference between Fig. 9 and 10 is primarily within that layer. The longshore velocity in the present case extends to the coastal wall, and

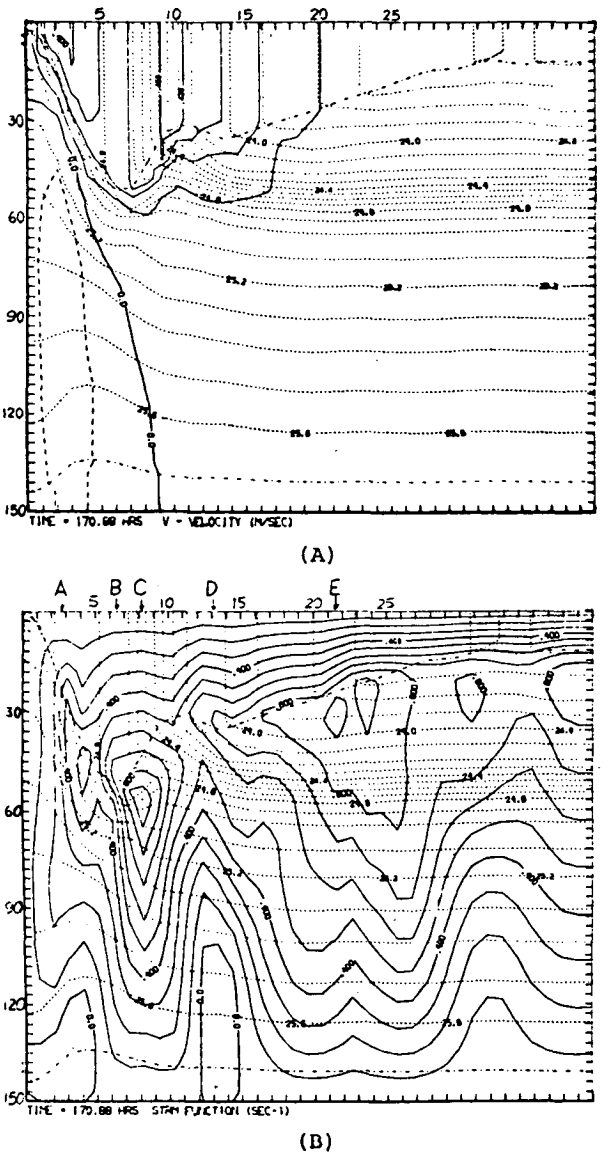


FIG. 8. The flow pattern for case I at 170.9 h.

the mixed layer immediately adjacent to the coast is deeper due to vertical mixing. The upwelling region is more concentrated at the coast, especially in the deeper layers. A large part of the crossfront circulation behaves like a boundary current and stays along the bottom, sidewall and surface boundaries. The counterclockwise circulation near the coast disappears. This free-slip circulation pattern induces a narrower and stronger upwelling than the no-slip case. The density surfaces rise an average of 20 m along the coast in 102 h compared to 10 m for the no-slip boundary condition. The interior stable layer reaches the mixed layer at 102 h forming a surface front. Turbulent mixing is indicated by the dip of the density surfaces. In the no-slip case, it takes another 30 h for the interior stable layer to surface.

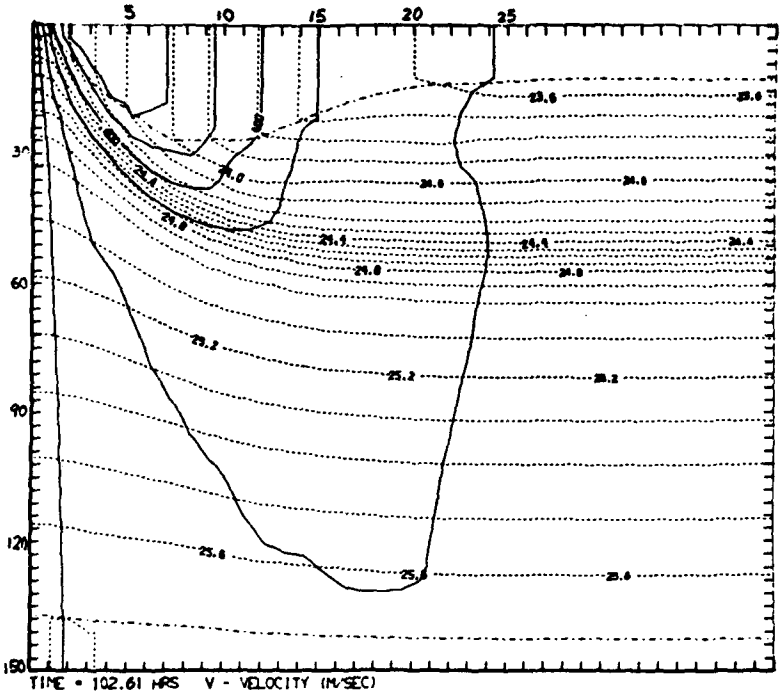


(A)

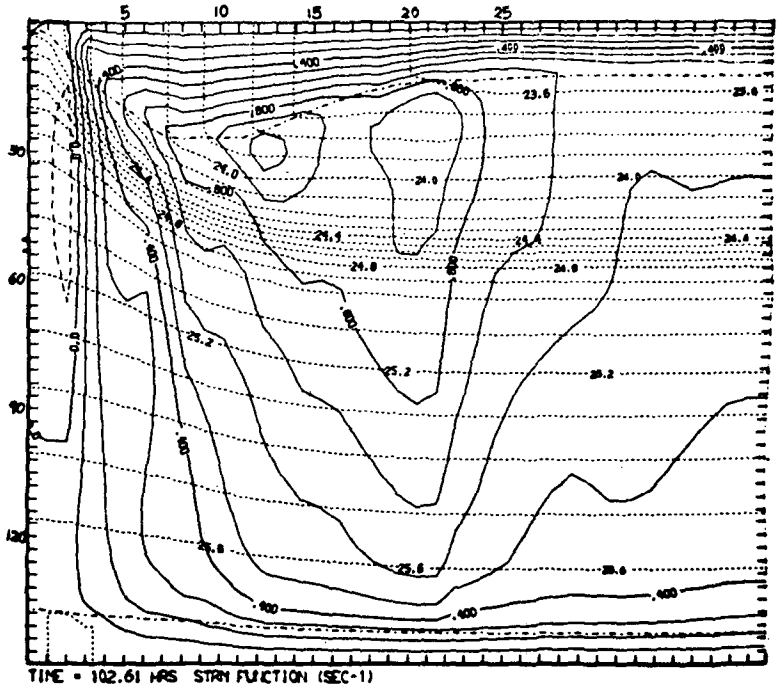


(B)

FIG. 9. The flow pattern for case II at 102.6 h. A background barotropic longshore velocity exists in this $f$-plane case.

From the above three cases, different crossfront circulation patterns emerge due to various boundary conditions. However, in the vicinity of the longshore jet and away from physical boundaries, all three cases show similar closed circulation patterns. This suggests that these boundary conditions have little effect in our region of interest, where nonlinear advection and turbulent mixing are dominant.

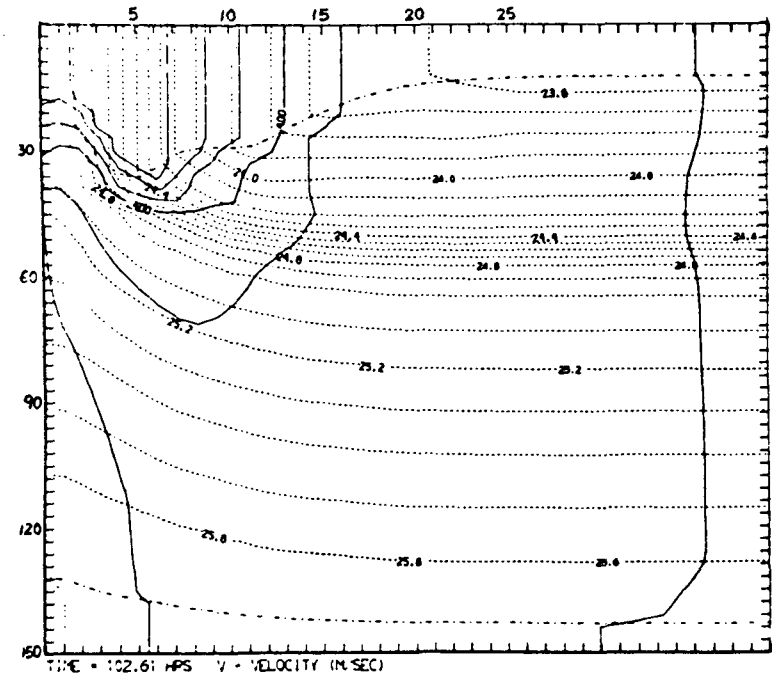


(A)

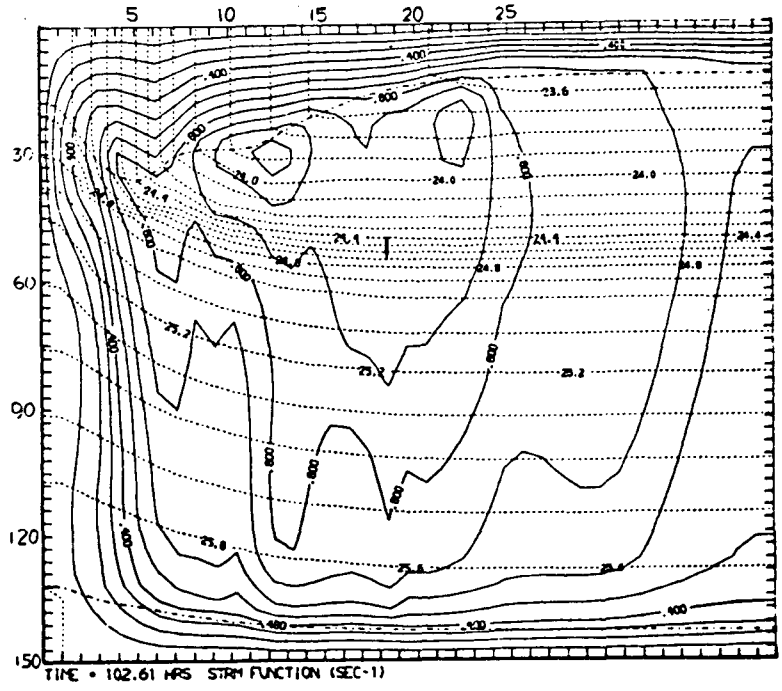


FIG. 10. The flow pattern for case III at 102.6 h. Free-slip boundary allows longshore velocity to accelerate at the coast.

*d. Case IV: Sloping no-slip case*

A linear sloping bottom is added which gives a barotropic velocity over the shallower region in the $\beta$-plane case. However, its effect on the cross shelf circulation is limited to the bottom boundary inflow, the secondary circulation in the frontal region is not affected.

Fig. 11 shows the flow pattern at 200 h. Comparing this case with case I (see Figs. 8 and 11), the basic flow pattern is the same. The similarities in these two figures can be summed up as follows: 1) a surface

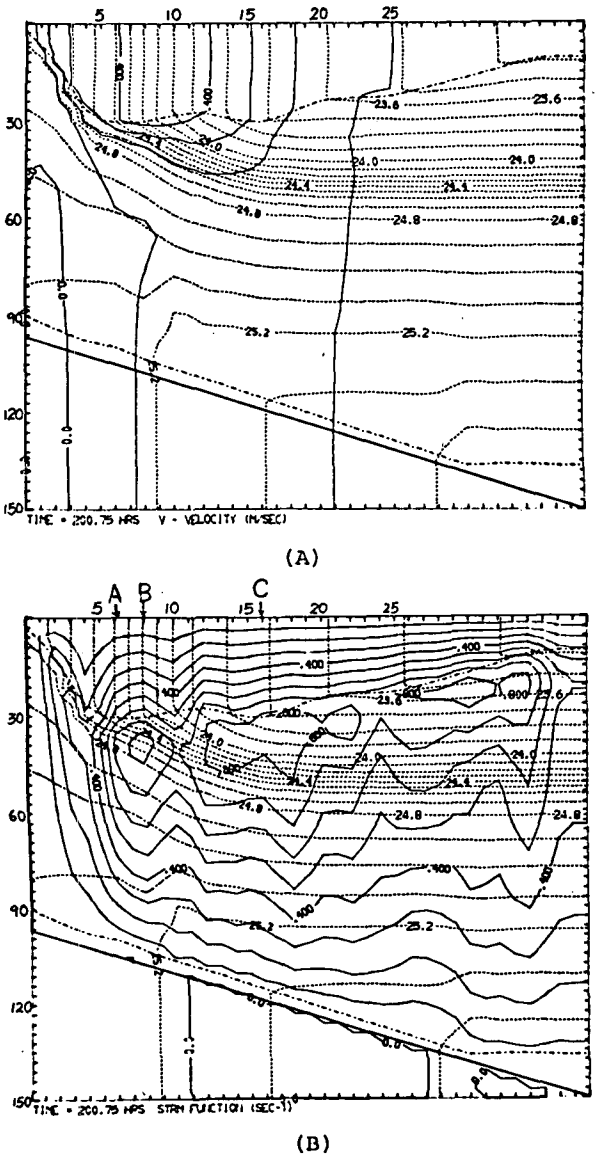


FIG. 11. The flow pattern for case IV at 200.8 h.

front is formed. 2) The mixed-layer depth has a maximum at point A at the inshore side of the surface front corresponding to B in Fig. 8. 3) The turbulent mixing occurs primarily between point A and the coast. 4) Two closed circulations centered at B and C correspond to C and E in Fig. 8. 5) Upwelling is also split into three branches located at similar locations in both figures.

### c. *Case V: Munk and Anderson's eddy coefficient formula*

Using a Richardson number related formula, the eddy coefficient is non-negligible over the area where velocity shear exists. Vertical mixing is important over the whole model domain and the difference induced by such an eddy coefficient change is dramatic (cf. Figs. 11 and 12). Outside of the upwelling zone, the eddy coefficient in the entrainment zone has an averaged value of 5 $cm^2\ s^{-1}$ due to the shear of Ekman transport. Inside the upwelling zone, the eddy coefficient has an average value of 25 $cm^2\ s^{-1}$ near the mixed layer and decreases gradually downward (see Fig. 13).

Strong vertical mixing over a broad region is indicated by the following phenomena at 200 h:

1) The mixed layer is ~15 m deeper than in case IV over most of the model domain.

2) The surface density outside the upwelling zone is increased mainly by vertical mixing.

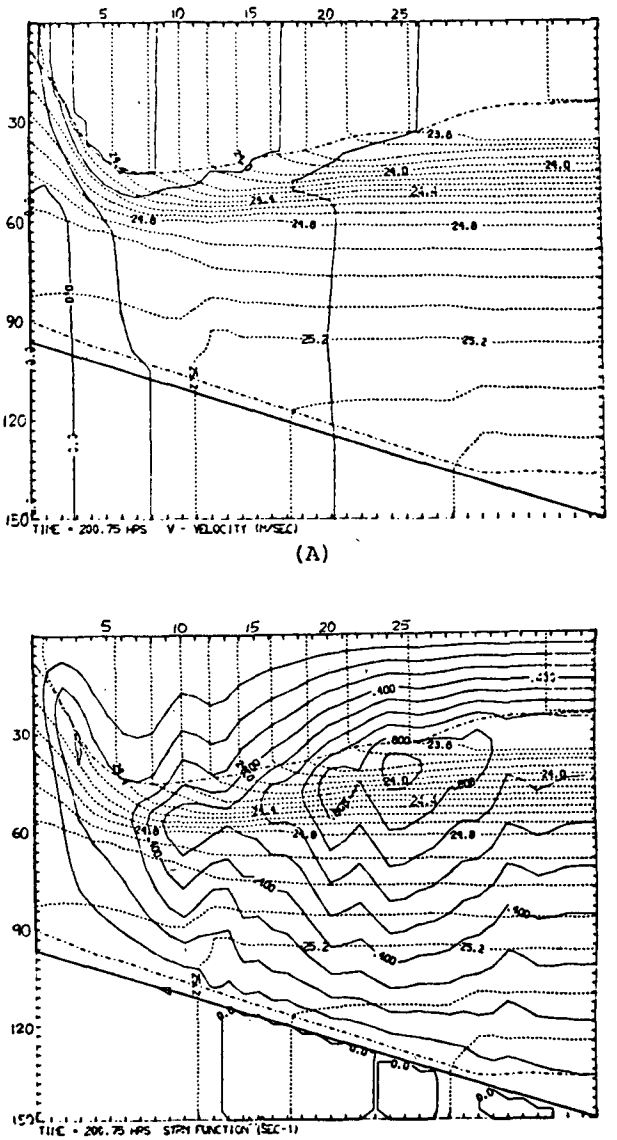


FIG. 12. The flow pattern for case V at 200.8 h. All the conditions are chosen similar to case IV except that the vertical eddy coefficient is determined by Munk and Anderson's formula. The circulation is much diffused.

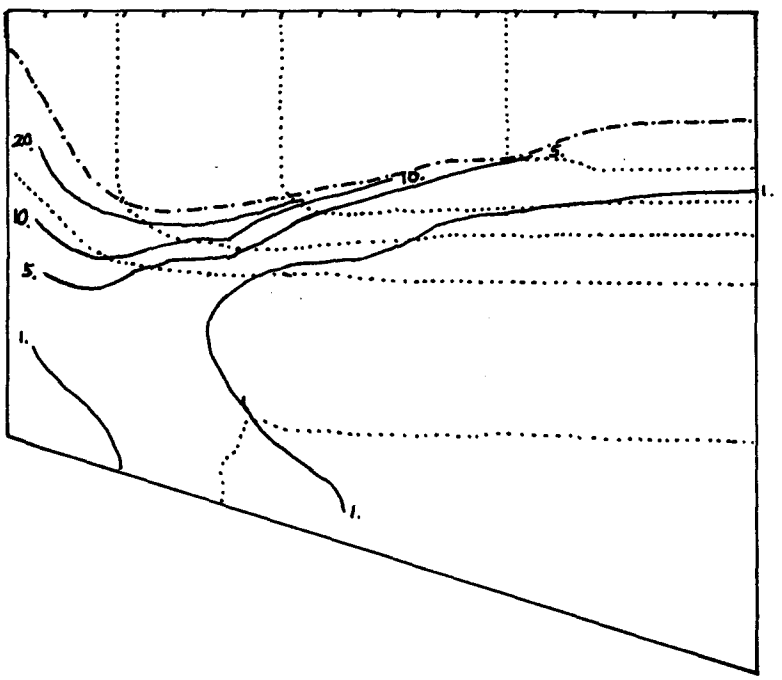


FIG. 13. Distribution of eddy viscosity $K_M$ at 200.8 h (case V). The dotted curves represent density surfaces; the uneven dashed curve represents the base of the mixed layer; solid curves indicate areas where $K_M$ is larger than 1, 5, 10 and 20 cm$^2$ sec$^{-1}$.

3) The interior density surfaces are diffused downward and piled on top of the interior stable layer.

4) The counterbalance between the upwelling of cold water and the downward diffusion of heat keeps the interior density surfaces horizontal. Interior density surfaces show a frontal structure only within 8 km from the shore.

5) The interior density surfaces are entrained into the surface layer by convection and mixing rather than by upwelling. This generates a widely spread density gradient without a surface front.

Water upwells over a width of 20 km, covering the whole frontal zone. Most of the surface transport upwells on the offshore side of the jet center, while in case IV most of the surface transport upwells on the inshore side of the jet center. The crossfront circulation has a much broader and more diffused pattern than that shown in Fig. 11. The lack of an extended interior frontal structure is indicated by the longshore current. On the offshore side of the jet center, the horizontal density gradient exists primarily in the mixed layer. The density surfaces are horizontal in the interior; hence, no baroclinic shear develops in the interior. The vertical shear is confined to a very thin layer beneath the mixed layer. The core of the current remains close to the coast and its magnitude drops 25% compared to case IV. The velocity pattern looks similar to a two-layer ocean with most of the structure in the upper layer displaced horizontally.

## 4. Discussion

The results presented in the previous chapter show differences in the overall upwelling pattern resulting from the conditions imposed in each case. Sidewall friction, topography and large-scale adjustment all affect the circulation pattern. However, certain features can be found in the upwelling zone from one case to another. These features are related to the frontal-scale dynamics and are relatively unaffected by the boundary conditions and large-scale dynamics.

By using the moment closure turbulence model, the results show not only sharp boundaries between the turbulent and quiescent regions, but also a sharp transition in time from the inviscid to the turbulent stage. The circulation patterns are quite different after the onset of shear instability and turbulence in the interior.

In the inviscid stage, one major mechanism affecting the frontal scale circulation is the nonlinear advection. Pedlosky (1978) predicts frontogenesis within a few days through the nonlinear feedback mechanism. The vertical velocity along the coast decreases the local stratification by stretching the water column. Therefore, the radius of deformation decreases which further increases the vertical velocity. Finally, the vertical velocity over a finite depth increases without restraint and forms a surface front at the coast. However, this process does not take place in this study. This discrepancy can be explained by

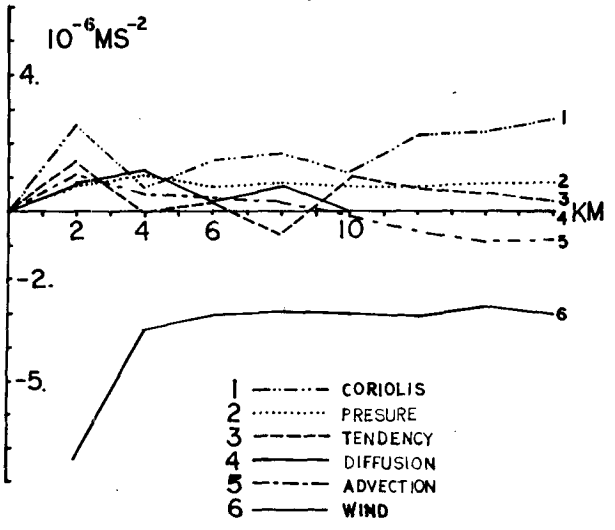


FIG. 14. The magnitude of each individual term of Eq. (4.1) ($v$ momentum equation) in the mixed layer at 200.8 h (case IV) as a function of offshore distance.

the following reasons as suggested by Pedlosky (1978). First of all, the upwelling region, which is defined as the area where the interior fluid penetrates into the mixed layer, has some finite width. Even with a free-slip coastal wall, the horizontal resolution at the coast is too coarse to confine the upwelling region to an infinitesimal area. Furthermore, with the intensification of the coastal jet, secondary upwelling regions develop away from the coast. Second, because of the surface layer, convective mixing may occur as the dense water advects offshore. This process changes the momentum, density and potential vorticity of the near surface flow. The interior density surface moves offshore with the surface transport, taking the coastal jet with it, rather than staying at the coast. Therefore, once this surface layer is included and allowed to interact with the interior, the alongshore momentum and density will not stay along the coast to form a front.

When the progressive tilting of the isopycnal causes the shear instability to occur on the inshore side of the jet, turbulence develops which changes the frontal scale circulation pattern. As first suggested by Csanady (1972), the interior vertical momentum mixing will affect the thermal wind balance and induce double Ekman layers. Wroblewsky (1977) generates the double-cell circulation based on this process. Johnson (1980) suggests the same mechanism as responsible for the double cell structure with some modification. In the present study, strong mixing occurs at the base of the mixed layer. With the downward diffusion of the longshore momentum, a relatively onshore flow develops in the mixed layer with offshore flow in the layers below. However, such a process cannot explain the clockwise circulation under the surface front. A double Ekman layer can only redistribute the crossfront transport vertically rather than generate a streamfunction maximum. Additional dynamical processes must take place simultaneously during the turbulent mixing.

In order to understand the mechanism of generating the closed circulation under the surface front, a diagnostic study is carried out at 200 h on case IV (see Fig. 11) in the mixed layer. The longshore momentum equation in the mixed layer is

$$\underset{3}{\frac{\partial v_k}{\partial t}} = \underset{5}{-u_k \frac{\partial v_k}{\partial x}} - \underset{2}{\frac{1}{2}\left(\frac{\partial M_k}{\partial y} - \frac{p_k}{\rho_S^2}\frac{\partial \rho_S}{\partial y}\right)} + \underset{6}{\frac{\tau_y}{\rho h'_{k+1}}} + \underset{4}{\frac{\overline{w'v'_{k+1}}}{h'_{k+1}}} - \underset{1}{fu_k} + A_M \frac{\partial^2}{\partial x^2} . \quad (4.1)$$

Underlines and numbers show the terms represented by each curve in Fig. 14; $v_k$ is the longshore velocity and $u_k$ the cross-front velocity. Curve 6 represents the momentum input by the flux across the interface between the mixed layer and the interior. It shows considerable mixing from the coast to 8 km offshore. Curve 3 represents the tendency term, which is strongly affected by the turbulent mixing. It drops in the region where curve 4 is positive. Curve 2 represents the longshore pressure gradient which is basically the $\beta$-plane adjustment. Curve 5 represents nonlinear advection; it indicates the effect of decreasing $v_k$ on the inshore side of the jet and increasing $v_k$ on the offshore side. It is the driving force for the closed circulation in Fig. 7. Curve 1 is the Coriolis term, which is proportional to the $u_k$ velocity. According to the double Ekman layer argument, a decrease of $v_k$ will decrease $u_k$. Curves 1 and 3 should then show the same pattern. However, between 6 to 10 km offshore, these two curves change more or less in opposite directions, i.e., $u_k$ velocity is large in the region where $v_k$ is decreasing with time and small in the region where $v_k$ increases. Thus, additional dynamics are involved in the $u_k$ momentum equation in addition to the change in $fv_k$.

Fig. 15 shows the magnitude of terms in the $u$ momentum equation in the mixed layer:

$$\underset{1}{\frac{\partial u_k}{\partial t} + u_k \frac{\partial u_k}{\partial x}} = \underset{2}{\frac{1}{2}\left(\frac{\partial M_k}{\partial x} - \frac{p_k}{\rho_S^2}\frac{\partial \rho_S}{\partial x}\right)} + fv_k + \frac{\overline{w'u'_{k+1}}}{h'_{k+1}} + A_M \frac{\partial^2 u_k}{\partial x^2} . \quad (4.2)$$

Only the tendency term and the difference of the first two terms on the right-hand side are shown in Fig. 15. Curve 1 gives the tendency term, curve 2 gives

the deviation from geostrophic balance. From Fig. 14, we find that the tendency term for $v$ is insignificant 4 km offshore. However, $v_k$ is still supergeostrophic as shown in Fig. 15. At 10 km offshore, the $v_k$ velocity increases with time but it remains subgeostrophic. Therefore, the $u_k$ velocity increases between 4 and 6 km and decreases 10 km offshore. This suggests that the pressure gradient also is changed by the turbulent mixing.

Fig. 16 shows the total velocity shear and the geostrophic velocity shear in the coastal jet. The geostrophic velocity shear is determined by the difference of the first term on the right-hand side of (4.2) between the surface and bottom mixed layer. These two curves indicate a super-geostrophic shear on the inshore side of the jet. Between 4 and 8 km offshore, the discrepancy increases. The geostrophic velocity shear even shows a decrease between 4 and 6 km. This indicates that the strong mixing between 4 and 8 km actually decreases the total baroclinic pressure gradient of the water column in this region.

With a flat bottom and Cartesian coordinate, the following argument can be carried out. Vertical mixing can only redistribute the density field but cannot change the mass of the water column. By integrating the thermal wind relation, the geostrophic shear of a water column equals the horizontal gradient of the total mass, i.e.,

$$\Delta v = \frac{\partial P}{\partial x}\bigg|_{\text{surface}} - \frac{\partial P}{\partial x}\bigg|_{\text{bottom}} = \frac{\partial \text{mass}}{\partial x} .$$

Therefore, the localized mixing cannot change the geostrophic shear directly. The following conceptual model is proposed for the dynamic process.

Assume that a region with constant stratification (see Fig. 17a) and that the associated geostrophic current has a constant shear as shown in Fig. 17b. Suppose that localized turbulence occurs at column B. Then, the vertical density structure at this column changes from a straight line to the thick curve as shown in Fig. 17c. The density increases near the surface and decreases in a lower region. The geostrophic adjustment due to such a local process will affect the horizontal density gradient over a wider region. Therefore, thermal wind relation is affected throughout the whole region. At two chosen depths, the horizontal density gradients change from the straight dashed lines to the solid curves as shown in Fig. 17a. The geostrophic shear at column C associated with this new density gradient increases near the surface and decreases in a lower region. Since the total geostrophic shear is unchanged, the geostrophic velocity has a shape shown by the dashed curve in Fig. 17b. In order to conserve the momentum of the column C, barotropic adjustment takes place to induce a surface pressure field. The whole curve shifts to the right as shown by the solid curve. The actual velocity, which is the straight thin line, becomes supergeostrophic at the upper layers and turns away from column B, while at the lower layers, it becomes subgeostrophic and turns towards column B. At column A, the whole process is reversed. As a result, the upper layers diverge and the lower layers converge. Strong upwelling develops at the location of strong downward mixing, see Fig. 17a. Superimpose this with the clockwise coastal circulation, and only the clockwise closed circulation under the surface front emerges.

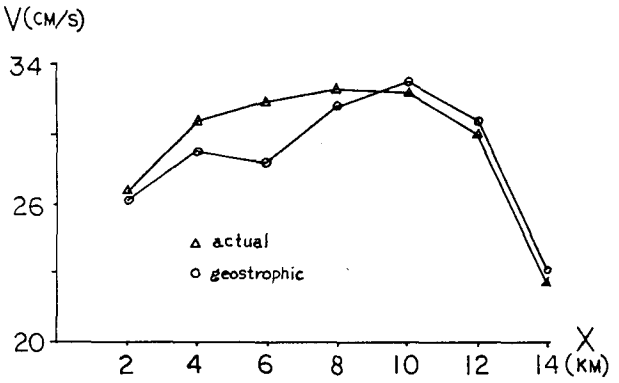


FIG. 16. The curves of actual velocity shear (Δ) and of geostrophic velocity shear (O) as functions of offshore distance at 200.8 h of case IV.

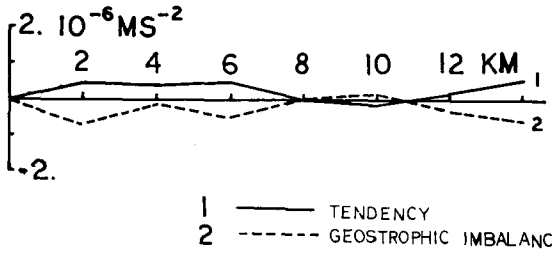


FIG. 15. As in Fig. 14 except that the magnitude of the tendency term and the geostrophic imbalance are shown for Eq. (4.2) ($u$ momentum).

As the major upwelling moves offshore with the turbulent region at the inshore side of the front, the total mass of the water column increases at its offshore side. Therefore, geostrophic shear decreases at its inshore side as shown in Fig. 8. It is this development of offshore upwelling regions that causes the coastal jet to split.

Case V is the only case using Munk and Anderson's eddy coefficient formula. It shows frontal structure quite different from the other cases. The major differences can be summed up as follows:

1) Density front: in the other cases, the interior front can be traced to the surface front; in case V, the interior density structure is largely distorted and no surface front is obtained.

2) Crossfront circulation: in the other cases, most

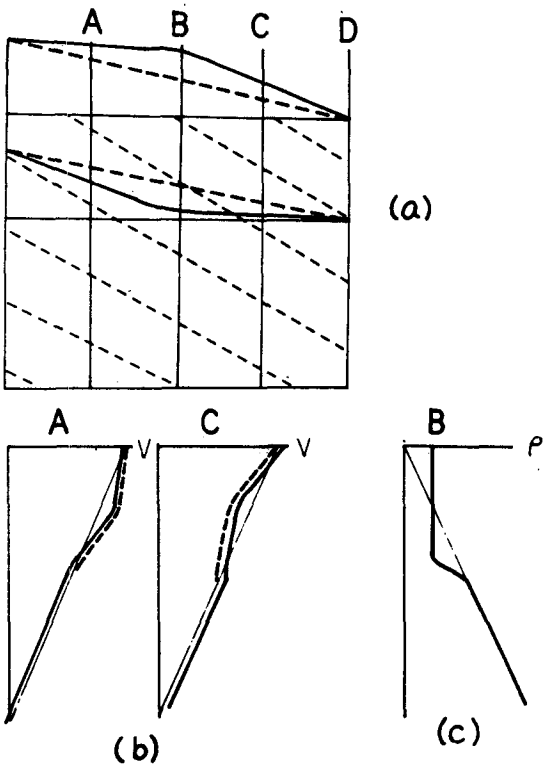


FIG. 17. The geostrophic adjustment around a localized vertical mixing maximum. (a) The density structure of the area of interest. The thin dashed lines represent the density surfaces. The thick dashed lines indicate the original horizontal density gradient at two chosen depths. The solid thick curves indicate the horizontal density gradient after the turbulent mixing at column B. (b) The velocity gradient at columns A and C, where the solid thin lines are the actual velocity. The dashed curves are the geostrophic shear. The solid thick curves indicate the geostrophic shear after adjustment of total momentum. (c) The density structure at column B, where the thin curve indicates the initial structure. The thick curve indicates the structure after turbulent mixing.

of the upwelling takes place on the inshore side of the coastal jet; in case V, most of the upwelling takes place on the offshore side of the jet.

3) Longshore current: case V shows a current intensity 25% weaker than the other cases.

These differences suggest that the mixing process is a very important mechanism for creating a frontal structure. Comparing Figs. 11 and 12, the velocity and density field deviate considerably from each other above the 25.0 $\sigma_t$ surface. Fig. 18 shows the eddy coefficient distribution corresponding to the time of Fig. 11. The turbulence event is confined to a limited region. The solid line indicates areas where the eddy coefficient is $>1$ cm$^2$ s$^{-1}$. Fig. 13 shows the eddy coefficient distribution corresponding to the time of Fig. 12. The Munk and Anderson formula gives strong mixing throughout the upwelling zone. These differences in eddy coefficients between Figs. 18 and 13 are responsible for the different flow patterns in Figs. 11 and 12.

Hamilton and Rattray (1978) (hereafter referred to as HR) formulated a continuously stratified model using Cartesian coordinates. Cases run by HR with Munk and Anderson's formula (Fig. 19) show a density structure very similar to that of case V (Fig. 12). The density difference over the whole water column for one of their cases (Fig. 19a) is $2 \times 10^{-3}$ g cm$^{-3}$, which is comparable to that of case V. The final density structure after 10 days forced by a 1 dyn cm$^{-2}$ wind stress shows the following features which are similar to those observed in case V at 200 h (Fig. 12). First of all, the general density structures are similar. The depth of the density surfaces in the upper layer increases toward the coast before the surfaces turn vertical in the mixed layer. The mixed layer deepens to 30 m far offshore and to 50 m near the center of the coastal current. Most of the interior frontal structure exists on the inshore side of the mixed layer thickness maximum. The surface density far offshore increases $\sim 0.4$ $\sigma_t$.

The major discrepancy occurs in the crossfront circulation pattern. HR shows a stronger boundary-layer current along both the bottom and the coastal wall than case V. The vertical velocity is confined mostly to within 5 km offshore and has a magnitude of $1.5 \times 10^{-2}$ cm s$^{-1}$, while the vertical velocity in case V shows a weaker and broader structure. In case V, vertical velocity reaches a magnitude of $1 \times 10^{-2}$ cm s$^{-1}$ within 2 km offshore and drops to $5 \times 10^{-3}$ cm s$^{-1}$ over a 10 km span centered $\sim 13$ km offshore. However, the discrepancy is largely caused by the $f$-plane assumption used by HR and the $\beta$-plane assumption and used in case V. The comparison between cases I and II suggests that the upwelling pattern is quite different for these two assumptions.

When using the moment closure turbulence model, the active mixing no longer occurs over the whole mixed layer; the turbulence region becomes localized. The case studies show that the upwelling current is influenced by turbulent mixing. Thus, upwelling fluid is confined to narrow regions. For instance, Fig. 11 shows that 50% of the upwelling water is confined to within one grid interval centered around 5 km offshore. The vertical velocity has a maximum of $1.8 \times 10^{-2}$ cm s$^{-1}$ (15.5 m day$^{-1}$). This lifting of water can greatly increase the local nutrient concentration in the euphotic zone and consequently form high productivity patches.

Recent emphasis has been placed on the three-dimensional irregularities of the upwelling phenomena, especially the existence of patches of low temperature or high productivity water plumes. Topographic irregularities in the longshore direction on the scale of the internal radius of deformation are most likely to affect a zonal structure by conserving potential vorticity. Stuart and Nanney (1978) gathered the surface temperature information to show patches of temperature minima along the coast

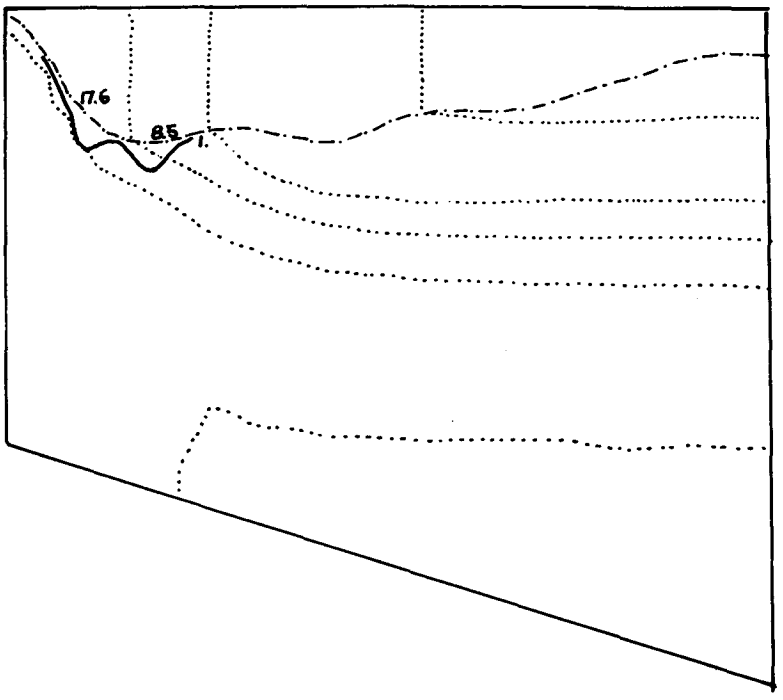


FIG. 18. As in Fig. 13 except that $K_M$ of case IV is shown. The solid curve indicates the region where $K_M$ is $>1$ cm$^2$ s$^{-1}$. The numbers indicate the maxima of $K_M$ in cm$^2$ s$^{-1}$.

of Peru on the leeside of seamounts. Preller and O'Brien (1980) simulated this pattern with a numerical model. Killworth (1978) solved an analytical problem with a wavelike coastline. It is the topographically trapped Kelvin or shelf waves induced by the passing zonal current that generates the localized upwelling extrema.

On the other hand, propagating Kelvin and shelf waves may be generated by wind forcing or the instability of the frontal current. Hoskins (1975) found that a front formed in the low-pressure region of an unstable wave due to ageostrophic advection of vorticity. Therefore, separate segments of a sharp front may develop in the inshore region of a single repeated wavetrain. With the superposition of amplifying waves in the longshore current, upwelling intensity will be amplified in certain selected regions.

## 5. Conclusion

Frontal-scale circulation is usually forced by an imbalance of the thermal wind relation. Recent two-dimensional numerical studies dealing with the frontal circulation of coastal upwelling focus on the following two aspects for inducing imbalance: 1) nonlinear advection of the frontal structure by the Ekman transport. Suginohara (1977) and Matsuno *et al.* (1978) simulate a complicated frontal circulation by assuming a surface front initially. The formation of the multiple closed circulations and localized frontogenesis is attributed to the nonlinear advection in the surface region. 2) Vertical diffusion of the longshore momentum. Wroblewsky (1977) [using Thompson's (1974) model] and Endoh (1977) generate a double-cell circulation from this process.

In the present study, frontal circulation is induced basically by the same two processes but in a more comprehensive way. Additional features have been included in the present model. First, the eddy coefficients of density and momentum are given the same order of magnitude. Second, sharp boundaries may exist at the spatial changes of these coefficients. As a result, two important interrelated phenomena reveal that 1) surface mixing is not as uniform as the wind stress, localized turbulent region forms within the frontal zone due to spatial variation of velocity and density; and 2) localized turbulent mixing changes the thermal wind relation not only by vertical diffusion of longshore momentum but also by modifying the horizontal density gradient. As a result, the localized upwelling develops at the region of strong turbulent mixing and a surface front forms at its offshore side with a clockwise circulation underneath.

Some numerical models (Endoh, 1977; Suginohara, 1977; Matsuno *et al.*, 1978) apply a weak heat diffusion coefficient to maintain the sharp density structure. In this model, the sharp pycnocline is either maintained by weak diffusion or intensified by strong turbulence. Sharp gradients of turbulent mixing (cf.

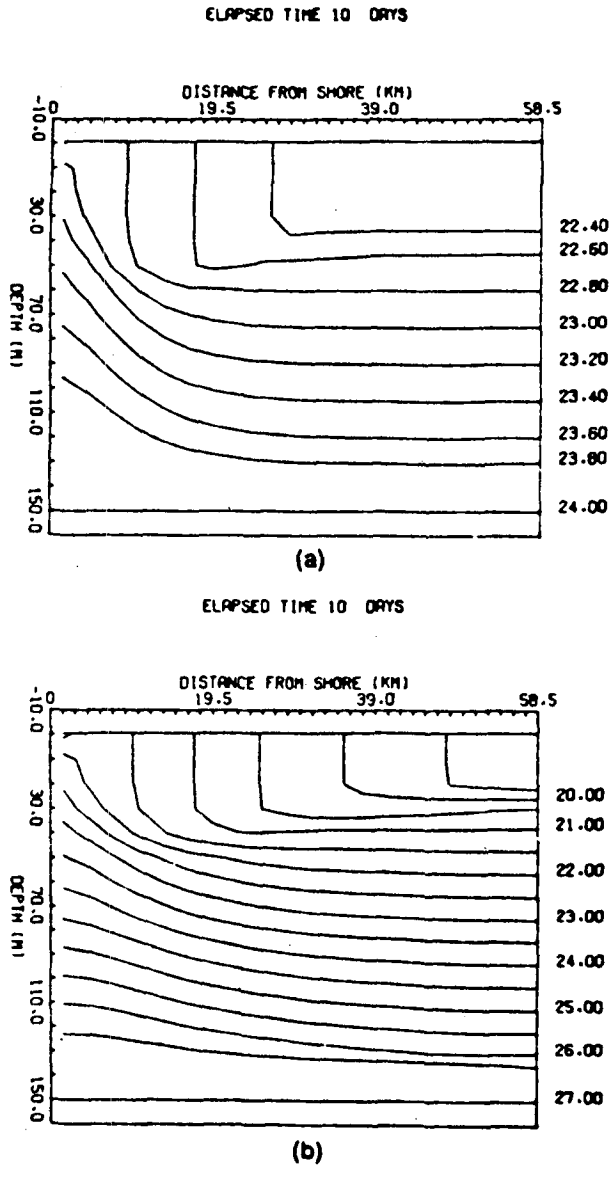


FIG. 19. Isopycnal distributions after 10 days of wind ($\tau_y$ = 1 dyn cm$^{-2}$) with $A_M = A_H = 10^5$ cm$^2$ s$^{-1}$ and $K_M$ and $K_H$ determined from Munk's formula. (a) $\Delta\rho = 2 \times 10^{-3}$ g cm$^{-3}$, (b) $\Delta\rho = 8 \times 10^{-3}$ g cm$^{-3}$ (reproduced from Hamilton and Rattray, 1977).

cases IV and V) help to intensify a surface front rather than diffuse it. Therefore, knowledge of the intensity of density diffusion is not enough to determine the diffusive effect; spatial distribution also is an important factor.

Another important process involved in the spatial distribution of vertical mixing is even more intriguing—the effect of vertical density diffusion on the thermal wind relation. During the turbulent mixing, not only the longshore momentum but also heat is diffused downward. When there is a horizontal gradient of turbulence intensity, the vertical density structure will change in the turbulent region at different rates, which changes the horizontal density gradient. Therefore, the vertical mixing of density can influence the thermal wind relation in the two-dimensional case. As a result, a localized, turbulent region induces a divergent field in the mixed layer and therefore, upwelling from below. This divergent field and its upwelling current will have the same effect as those induced by wind along the coast. The longshore jet intensifies at the offshore side and weakens at the inshore side.

However, these results should not be considered as quantitative representations of what happens to coastal upwelling in nature. It merely demonstrates the complicated processes involved when a more comprehensive turbulence distribution is implemented. Due to the lack of understanding of turbulence processes in a high-energy region such as a frontal zone, the adoption of a one-dimensional turbulence model cannot give a complete picture of the mixing process.

Curtin's (1979) data showed the same dipping of density surface (as shown in Fig. 8) at the inshore side of the surface front during an upwelling event. It suggests that strong mixing takes place or has taken place in this region. Interior Richardson number calculations (Wang and Mooers, 1977; Curtin, 1979) suggests that instability occurs at the base of the pycnocline. Wave energy, both the inertial wave and the internal tide, decreases during mixing. Johnson (1981) finds the same region of instability in a wedge-shaped density field with strong emphasis on the relation between the Richardson number distribution and the density structure. However, the present study does not find turbulence at the pycnocline base. The discrepancy suggests that the wave field, which has maximum shear at pycnocline, is another energy source for turbulence. Background velocity and density fields generated by previous upwelling events are important, too.

The inertial energy generated at the surface and the internal tide generated at the shelf break are usually dissipated at the pycnocline. Turbulent diffusion must be involved. The inclusion of wave energy allows the turbulence region to be more diffused and to extend to the pycnocline.

Wedge-shaped density fields have been observed during the upwelling season off Oregon. They are formed by diabatic processes over a long period of time rather than adiabatically as in an analytical model. In an adiabatic and inviscid system, the potential vorticity is conserved. Curtin (1979) found that the potential vorticity had large spatial variations in the frontal zone. He shows an increase of potential vorticity both inshore and near the surface, which is due to surface mixing and near-shore surface heating. The wedge-shaped density structure is generated more likely by the diabatic heating on a series of upwelling and downwelling events than by

conservation of potential vorticity. Therefore, continuously stratified models fail to spin up a wedge-shaped structure from rest during one single upwelling event. The model fails to simulate the relaxation stage after an active upwelling period. The re-stratification of well-mixed layer by combination of horizontal density gradient and vertical shear of cross-shore flow in the mixed layer has not been properly modeled. This study minimized the boundary effect by imposing very simple boundary conditions and structure. Complications due to longshore or cross-shore variability are avoided.

*Acknowledgments.* This is part of my Ph.D. reserach at University of Miami. I am grateful for the guidance of Dr. Claes Rooth and Dr. Rainer Bleck, who were my advisors during the course of this work. I want to extend my appreciation to Dr. George Mellor for letting me use the turbulence model and to Dr. John Klinck for editing this manuscript.

This project is sponsored by the Office of Naval Research, under Grant N000-14-75-C-0173, and from the National Science Foundation, under Grants OCE77-26801 and ATM78-24396. The computational work was accomplished at the National Center for Atmospheric Research under Grant 35191009.

The final preparation is done at Florida State University with the support of the Office of Naval Research, under Grant N000-14-80-0076. Some of the results in this paper have appeared in another paper in the IDOE publication, International Symposium of Coastal Upwelling.

## APPENDIX A

## Governing Equations for the Boundary Layers

### 1. Bottom boundary layer

In the boundary layer, vertical shear does not exist and eddy coefficients are not defined. The vertical diffusion term has to be changed from a second order differential form to a first-order differentiation of the Reynolds flux. The governing equations are modified to

$$\frac{\partial u_m}{\partial t} + u_m \frac{\partial u_m}{\partial x} = A_M \frac{\partial^2 u_m}{\partial x^2} - \frac{C_d u_m^2 + \overline{w'u_m'}}{(D - h_m')} - \frac{\partial M_m}{\partial x} + \frac{P_m}{\rho_B^2}\frac{\partial \rho_B}{\partial x} + fv_m, \quad \text{(A1)}$$

$$\frac{\partial v_m}{\partial t} + u_m \frac{\partial v_m}{\partial x} = A_M \frac{\partial^2 v_m}{\partial x^2} - \frac{C_d v_m^2 + \overline{w'v_m'}}{(D - h_m')} - \frac{\partial M_m}{\partial y} + \frac{P_m}{\rho_B^2}\frac{\partial \rho_B}{\partial y} - fu_m, \quad \text{(A2)}$$

$$\frac{\partial \rho_B}{\partial t} = -\frac{\overline{w'\rho_m'}}{(D - h_m')} - u_m \frac{\partial \rho_B}{\partial x}, \quad \text{(A3)}$$

$$\frac{\partial P_m}{\partial t} = \frac{\partial \rho_B}{\partial t}\frac{\partial P}{\partial \rho}\bigg|_{P_m} = \frac{\partial \rho_B}{\partial \rho}\frac{P_m - P_{m-1}}{\rho_B - \rho_{m-1}}, \quad \text{(A4)}$$

$$h_m = P_m \rho_B^{-1}. \quad \text{(A5)}$$

Here subscript $m$ is the vertical index of the bottom boundary layer and $C_d$ is the bottom drag coefficient. The Reynolds fluxes are defined as

$$\overline{w'u_m'} = K_{Mm}\frac{u_m - u_{m-1}}{h_m - h_{m-1}} = K'_{Mm}\frac{u_m - u_{m-1}}{\rho_B - \rho_{m-1}}, \quad \text{(A6)}$$

$$\overline{w'v_m'} = K_{Mm}\frac{v_m - v_{m-1}}{h_m - h_{m-1}} = K'_{Mm}\frac{v_m - v_{m-1}}{\rho_B - \rho_{m-1}}, \quad \text{(A7)}$$

$$\overline{w'\rho_m'} = K_{Hm}\frac{\rho_m - \rho_{m-1}}{h_m - h_{m-1}} = K'_{Hm}. \quad \text{(A8)}$$

Eqs. (A1) and (A2) are the momentum equations in the bottom mixed layer. The second and third term on the right-hand side are the forcing due to bottom friction and interface momentum flux, respectively. They are considered as body forces so that the vertical differentiation is represented by dividing with the layer thickness, $(D - h_m')$, which is the distance between the bottom and the depth at the midpoint of the top of the bottom mixed layer and the adjacent interior grid. The fifth term on the right-hand side is an extra term for the acceleration potential due to the existence of a horizontal density gradient in the bottom mixed layer. Eq. (A3) predicts the mixed-layer density change from the interface heat flux and the lateral advection of heat. Eqs. (A4) and (A5) predict the changes of the mixed-layer pressure and thickness.

### 2. Surface boundary layer

The governing equations for the surface boundary layer may be written as

$$\frac{\partial u_k}{\partial t} + u_k\frac{\partial u_k}{\partial x} = A_M\frac{\partial^2 u_k}{\partial x^2} + \frac{(\tau_x/\rho + \overline{w'u_{k+1}'})}{h'_{k+1}} - \frac{1}{2}\left(\frac{\partial M_k}{\partial x} - \frac{P_k}{\rho_S^2}\frac{\partial \rho_S}{\partial x}\right) + fv_k, \quad \text{(A9)}$$

$$\frac{\partial v_k}{\partial t} + u_k\frac{\partial v_k}{\partial x} = A_M\frac{\partial^2 v_k}{\partial x^2} + \frac{(\tau_y/\rho + \overline{w'v_{k+1}'})}{h'_{k+1}} - \frac{1}{2}\left(\frac{\partial M_k}{\partial y} - \frac{P_k}{\rho_S^2}\frac{\partial \rho_S}{\partial y}\right) - fu_k, \quad \text{(A10)}$$

$$\frac{\partial \rho_S}{\partial t} = \frac{Q + S_2\overline{w'\rho_{k+1}'}}{h'_{k+1}} - u_k\frac{\partial \rho_S}{\partial x}, \quad \text{(A11)}$$

$$\frac{\partial P_k}{\partial t} = S_3\frac{\partial \rho_S}{\partial t}\frac{\partial P}{\partial \rho}\bigg|_{P_k} = \frac{\partial \rho_S}{\partial t}\frac{P_{k+1} - P_k}{\rho_{k+1} - \rho_S}S_3, \quad \text{(A12)}$$

$$h_k = P_k \rho_S^{-1}. \quad \text{(A13)}$$

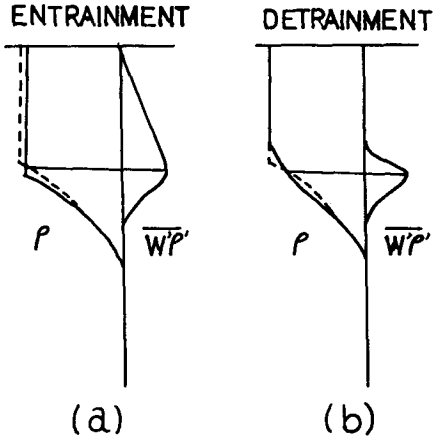


FIG. 20. The profiles of density flux in (a) an entrainment and (b) a detrainment stage. The dotted curves represent the initial density profiles. The solid curves on the left represent modified density profiles. The solid curves on the right represent the Reynold's flux.

Eqs. (A9) to (A10) are the momentum equations. Eq. (A11) is the thermodynamic equation, $Q$ is the surface heat input. Eqs. (A12) and (A13) predict the changes of mixed-layer pressure and thickness.

The coefficients $S_1$, $S_2$ and $S_3$ have two sets of values for the entrainment and detrainment stage separately. Therefore, special attention is needed to determine whether a state is in an entrainment or a detrainment stage.

The Reynolds flux generated in the entrainment zone does not indicate the direction of change of the mixed-layer depth. Fig. 20 demonstrates the entrainment and detrainment stages generated by the same Reynolds flux, $\overline{w'\rho'}$, in the entrainment zone. However, the mixed-layer depth can increase or decrease depending on the vertical gradient of $\overline{w'\rho'}$ which has different vertical profiles in the mixed layer. An additional condition is needed to determine the occurrence of entrainment or detrainment of the mixed layer. An integrated energy budget equation given by Niiler (1975) is adopted to diagnose the direction of mixed-layer depth change.

$$AP = 1.25u_*^3 - \left(\mu + B_0 + u_k \frac{\partial \rho_S}{\partial x} h_k\right)h_k \begin{cases} >0 \text{ (entrainment)} \\ <0 \text{ (detrainment).} \end{cases} \quad \text{(A14)}$$

Viscous velocity $u_*$ is defined as $(\tau/\rho)^{1/2}$, $B_0$ is the surface heating, the last term in the parenthesis is the horizontal advection of buoyancy. The variable $AP$ is only used as an indicator, its magnitude is not involved in later calculation. A positive value indicates that the turbulence induced by the surface stress and the buoyancy advected horizontally are large enough to saturate the mixed layer. The mixed layer will remain well mixed and its depth will increase. Excluded from the integrated equation is the shear production term which can be the driving force for either the entrainment or detrainment processes. A dissipation coefficient $\mu$ is included (Kim, 1976) which has its counterpart in the turbulence kinetic energy equation.

$$\mu \approx h_k^{-1} \int_0^{h_k} \frac{(q^2)^{3/2}}{B_1 l} dh, \quad \text{(A15)}$$

where $q^2$ is the turbulence energy, $l$ is the turbulence mixing length and $B_1$ is an empirical constant.

In the entrainment stage, the mixed layer is thoroughly turbulent. The upward transport of heat and momentum fluxes from the entrainment zone is working as a body force to change the density and momentum of the mixed layer. The increase of the mixed-layer depth is determined by matching the density of the mixed layer with the interior density profile. Therefore, the magnitudes of $S_1$, $S_2$ and $S_3$ are all set to one.

In the detrainment stage, the turbulence cannot be sustained over the whole mixed layer. The heat and momentum fluxes generated in the entrainment zone are used to erode the edge of the well-mixed layer back into the stratified interior. Since the density and momentum of the mixed layer are not affected by these fluxes, $S_1$ and $S_2$ are set to zero. The depth is decreased by

$$\frac{\partial h_k}{\partial t} = \frac{\partial \rho_S}{\partial t} SH, \quad \text{(A16)}$$

where $SH$ is the original density gradient. This assumption helps the density field to return to the initial profile during a relaxation period. Therefore, $S_3$ is set to $(\rho_{k+1} - \rho_S)/(P_{k+1} - P_k)SH$.

## APPENDIX B

### Determination of Turbulence Length Scale

Mellor and Yamada (1974) used a very simple empirical function to determine the turbulence length scale,

$$l_0 = \int q^2 h dh \left(\int q^2 dh\right)^{-1}, \quad \text{(B1)}$$

$$l = \kappa h(1 + \kappa h/l_0)^{-1}, \quad \text{(B2)}$$

where $\kappa$ is the von Kármán constant. The mixing-length scale $l$ increases linearly as $\kappa h$, in the constant stress layer and then increases asymptotically approaching $l_0$.

In this model, turbulent energy is not explicitly resolved in the mixed layer and $l_0$ is impossible to obtain. Therefore, $l$ has to be determined from several other length scales which are related to the overall turbulent integral length scale:

1) Near a physical boundary, the length scale is controlled by the existence of the boundary,

$$l_S = \kappa h, \tag{B3}$$

$$l_B = \kappa(D - h), \tag{B4}$$

where the water depth is $D$.

2) von Kármán defined a local length scale $l_V$ (Tennekes and Lumley, 1972) directly related to the local velocity structure, i.e.,

$$l_V = \frac{\partial u}{\partial h} \Big/ \frac{\partial^2 u}{\partial h^2}. \tag{B5}$$

3) Dickey (1977) examined the integral mixing length in an unforced decaying system and found that a critical maximum length scale existed for turbulence to be sustained,

$$l_D = (\mathrm{Ri}_c q^2/N^2)^{1/2}, \tag{B6}$$

where the critical Richardson number $\mathrm{Ri}_c = 5.43$ is determined empirically.

To define a length scale depending on all the above scales, the simplest form is chosen,

$$l = (l_S^{-1} + l_B^{-1} + l_V^{-1} + l_D^{-1})^{-1}. \tag{B7}$$

## APPENDIX C

### Separation of Barotropic and Baroclinic Modes

We separate the vertical variation of the horizontal velocity field into barotropic and baroclinic components:

$$u = u' + U,$$

$$v = v' + V,$$

$$U = (\rho g D)^{-1} \int u dP = (\rho g D)^{-1} \sum_{i=2}^{M} (u_i + u_{i-1}) \times (P_i - P_{i-1})/2 = (\rho g D)^{-1} \sum_{i=2}^{M} u_i \Delta P_i,$$

$$\sum_{i=2}^{M} (u_i' + u_{i-1}')(P_i - P_{i-L})/2 = \sum_{i=2}^{M} u_i' \Delta P_i = 0. \tag{C1}$$

By formally separating the momentum equation to give a prediction of each component, the surface elevation appears only in the prediction equation for the barotropic velocity. The surface pressure for the baroclinic component becomes zero. By redefining pressure and the Montgomery potential, we have

$$P' = P - g\eta,$$

$$M' = P'\rho^{-1} - gh,$$

where $\eta$ is the surface elevation. After the prime is dropped for convenience, the momentum equations become

$$\frac{\partial U}{\partial t} + U\frac{\partial U}{\partial x} + [A] - fV = A_M \frac{\partial^2 U}{\partial x^2} + g\frac{\partial \eta}{\partial x}, \tag{C2}$$

$$\frac{\partial V}{\partial t} + U\frac{\partial V}{\partial x} + [B] + fU = A_M \frac{\partial^2 V}{\partial x^2} + g\frac{\partial \eta}{\partial y}, \tag{C3}$$

$$\frac{\partial u}{\partial t} + u\frac{\partial u}{\partial x} + \frac{\partial Uu}{\partial x} + \dot{\rho}\frac{\partial u}{\partial \rho} - [A] - fv = -\frac{\partial M}{\partial x} + A_M \frac{\partial^2 u}{\partial x^2} + \frac{\partial \rho}{\partial h}\frac{\partial}{\partial \rho}\left(K_M \frac{\partial u}{\partial \rho}\right), \tag{C4}$$

$$\frac{\partial v}{\partial t} + u\frac{\partial v}{\partial x} + U\frac{\partial v}{\partial x} + u\frac{\partial V}{\partial x} + \dot{\rho}\frac{\partial v}{\partial \rho} - [B] + fu = -\frac{\partial M}{\partial y} + A_M \frac{\partial^2 v}{\partial x^2} + \frac{\partial \rho}{\partial h}\frac{\partial}{\partial \rho}\left(K_M \frac{\partial v}{\partial \rho}\right), \tag{C5}$$

$$[A] = \left\{\sum u\frac{\partial P}{\partial t} + \left[\sum \Delta P\left(U\frac{\partial u}{\partial x} + u\frac{\partial u}{\partial x} - A_M\frac{\partial^2 u}{\partial x^2} + \frac{\partial M}{\partial x}\right)\right](\rho g D)^{-1}\right\} + \frac{\tau_S^x - \tau_B^x}{\rho D},$$

$$[B] = \left\{\sum v\frac{\partial P}{\partial t} + \left[\sum \Delta P\left(U\frac{\partial v}{\partial X} + u\frac{\partial v}{\partial x} - A_M\frac{\partial^2 v}{\partial x^2} + \frac{\partial M}{\partial y}\right)\right](\rho g D)^{-1}\right\} + \frac{\tau_S^y - \tau_B^y}{\rho D},$$

where $\tau_S$, $\tau_B$ are the stresses at the surface and bottom and the superscript indicates direction.

## REFERENCES


Bleck, R., 1978: Simulation of coastal upwelling frontogenesis with an isopycnal coordinate model. *J. Geophys. Res.*, **85**, 6163–6172.

——, and D. Boudra, 1981: Initial testing of a numerical ocean circulation model using a hybrid (quasi-isopycnic) vertical coordinate. Submitted to *J. Phys. Oceanogr.*

Clancy, R. M., and P. J. Martin, 1979: The NORDA/FLENUMO-CEACEN thermodynamical ocean prediction system (TOPS): A technical description. NORDA Tech. Note 54, 82 pp.

Csanady, G. T., 1972: Frictional secondary circulation near an upwelled thermocline. Canadian Committee of Oceanography Symposium, Burlington, Ontario.

Curtin, T., 1979: Physical dynamics of the coastal upwelling front zone off Oregon. Ph.D. dissertation, University of Miami.

Denman, K. L., 1973: A time-dependent model of the upper ocean. *J. Phys. Oceanogr.*, **3**, 173–184.

De Szoeke, R. A., 1980: On the effects of horizontal variability of wind stress on the dynamics of the ocean mixed layer. *J. Phys. Oceanogr.*, **10**, 1439–1454.

Dickey, T., 1977: An experimental study of decaying and diffusing turbulence in neutral and stratified fluid. Ph.D. dissertation, Princeton University, 108 pp.

Endoh, M., 1977: Double-celled circulation in coastal upwelling. *J. Oceanogr. Soc. Japan*, **33**, 30–37.

Gargett, A. D., T. B. Sanford and T. R. Osborn, 1979: Surface mixing layers in the Sargasso sea. *J. Phys. Oceanogr.*, **9**, 1090–1111.

Garvine, R. W., 1974: Ocean interiors and coastal upwelling models. *J. Phys. Oceanogr.*, **4**, 121–125.

Garwood, R., Jr., 1977: An oceanic mixed layer model capable of simulating cyclic states. *J. Phys. Oceanogr.*, **7**, 455–468.

Halpern, D., 1976: Structure of a coastal upwelling event observed off Oregon during July 1973. *Deep-Sea Res.*, **23**, 495–508.

Hamilton, P., and M. Rattray, Jr., 1978: A numerical model of the depth-dependent, wind-driven upwelling circulation on a continental shelf. *J. Phys. Oceanogr.*, **8**, 437–457.

——, R. L. Smith and E. Mittelstaedt, 1977: Cross-shelf circulation on the continental shelf off Northwest Africa during upwelling. *J. Mar. Res.*, **35**, 787–796.

Hoskins, B. J., 1975: The geostrophic momentum approximation and the semi-geostrophic equation. *J. Atmos. Sci.*, **32**, 233–242.

——, and F. P. Bretherton, 1972: Atmospheric frontogenesis models, mathematical formulation and solution. *J. Atmos. Sci.*, **29**, 11–37.

Hurlburt, H. E., and D. Thompson, 1973: Coastal upwelling on a beta plane. *J. Phys. Oceanogr.*, **3**, 16–32.

Johnson, D. R., 1981: Double cell circulation during coastal upwelling. *Coastal Upwelling Research, 1980,* F. A. Richards, Ed., Amer. Geophys. Union (in press).

——, and W. R. Johnson, 1979: Vertical and cross-shelf flow in the coastal upwelling region off Oregon. *Deep-Sea Res.*, **26**, 399–408.

Johnson, W. R., J. C. Van Leer and C. N. K. Mooers, 1976: A cyclesonde view of coastal upwelling. *J. Phys. Oceanogr.*, **6**, 556–574.

Killworth, P. D., 1978: Coastal upwelling and Kelvin waves with small longshore topography. *J. Phys. Oceanogr.*, **8**, 188–205.

Kim, J. W., 1976: A generalized bulk model of the oceanic mixed layer. *J. Phys. Oceanogr.*, **6**, 686–695.

Kraus, E. B., and J. S. Turner, 1967: A one-dimensional model of the seasonal thermocline. Part II. *Tellus*, **19**, 98–105.

Mahrer, Y., and R. Pielke, 1978: A test of an upstream spline interpolation technique for the advective terms in a numerical mesoscale model. *Mon. Wea. Rev.*, **106**, 818–830.

Matsuno, K., K. Takeuchi and N. Suginohara, 1978: Upwelling front and two-cell circulation in a two-dimensional model. *J. Oceanogr. Soc. Japan*, **34**, 217–221.

Mellor, G. L., and P. A. Durbin, 1975: The structure and dynamics of the ocean surface mixed layer. *J. Phys. Oceanogr.*, **5**, 718–728.

——, and T. Yamada, 1974: A hierarchy of turbulence closure models for planetary boundary layers. *J. Atmos. Sci.*, **31**, 1791–1806.

Mooers, C. N. K., C. A. Collins and R. L. Smith, 1976: The dynamic structure of the frontal zone in the coastal upwelling region off Oregon. *J. Phys. Oceanogr.*, **6**, 3–21.

Munk, W. H., and E. R. Anderson, 1948: A note on the theory of the thermocline. *J. Mar. Res.*, **7**, 276–295.

Niiler, P. P., 1975: Deepening of the wind mixed layer. *J. Mar. Res.*, **33**, 405–422.

Orlanski, I., and B. B. Ross, 1977: The circulation associated with a cold front, Part I: Dry case. *J. Atmos. Sci.*, **34**, 1619–1633.

Pedlosky, J., 1978: A nonlinear model of the onset of upwelling. *J. Phys. Oceanogr.*, **8**, 178–187.

Pollard, R. T., P. Rhines and R. Thompson, 1973: The deepening of the wind-mixing layer. *Geophys. Fluid Dyn.*, **3**, 381–404.

Preller, R., and J. J. O'Brien, 1980: The influence of bottom topography on upwelling off Peru. *J. Phys. Oceanogr.*, **10**, 1377–1398.

Price, J. F., C. N. K. Mooers and J. C. Van Leer, 1978: Observation and simulation of storm-induced mixed-layer deepening. *J. Phys. Oceanogr.*, **8**, 582–599.

Roisin, B., 1980: Mixing, convection and advection in the upper ocean, Ph.D. dissertation, Florida State University, 195 pp.

Starr, V. P., 1945: A quasi-Lagrangian system of hydrodynamical equations. *J. Meteor.*, **2**, 227–237.

Stuart, D. W., and M. Nanney, 1978: Maps of mean sea surface temperature during Joint II 1976 and 1977. CUEA Synapse Notes. Vol. 4, No. 2 (unpublished report).

Suginohara, N., 1977: Upwelling front and two-cell circulation. *J. Oceanogr. Soc. Japan*, **33**, 115–130.

Tennekes, H., and J. L. Lumley, 1972: *A First Course in Turbulence*. The MIT Press, 300 pp.

Thompson, D., 1974: The coastal upwelling cycle on a beta plane, hydrodynamics and thermodynamics. Ph.D. dissertation, Florida State University, 141 pp.

Thompson, R. O. R. Y., 1976: Climatological numerical models of the surface mixed layer in the ocean. *J. Phys. Oceanogr.*, **6**, 496–503.

Wang, D. P., and C. N. K. Mooers, 1977: Evidence for interior dissipation and mixing during a coastal upwelling event off Oregon. *J. Mar. Res.*, **35**, 697–713.

Worthem, S., and G. Mellor, 1980: Turbulence closure model applied to upper tropical ocean. *GATE-1, Oceanography and Surface Meteorology in the B/C Scale*, Pergamon Press, 237–272.

Wroblewsky, J. S., 1977: A model of phytoplankton plume formation during variable Oregon upwelling. *J. Mar. Res.*, **35**, 357–393.